Rock Mechanics and Rock Engineering
https://doi.org/10.1007/s00603-024-04170-4

ORIGINAL PAPER

Temporal and Spatial Evolution of Non-Elastic Strain Accumulation in Stanstead Granite During Brittle Creep

Mehrdad Imani[1] · **Gabriel Walton**[2] · **Omid Moradian**[1,3] · **Ahmadreza Hedayat**[1]

Received: 31 January 2024 / Accepted: 10 September 2024

Abstract

Understanding the long-term behavior of brittle rocks requires fundamental consideration of time-dependent strain evolution and brittle creep processes. Previous studies have evaluated sub-critical crack growth during time-dependent deformation and damage evolution in brittle rocks; however, there is an incomplete knowledge of how damage evolves spatially and temporally within the body of intact rocks, where distributed regions of damage interact and coalesce during creep. This paper presents laboratory research focusing on evaluating brittle creep damage processes in Stanstead granite (SG) using 2-dimensional digital image correlation (2D-DIC). In the laboratory, the prismatic SG specimens were loaded beyond an estimated Crack Damage stress threshold (CD) level and then maintained a constant stress to initiate the creep process. DIC was used to characterize full-field spatiotemporal strain evolution, which was then interpreted in the context of local regions of "damage", determined according to a strain-based criterion. A method was proposed for identifying "existing" and "new" damage regions over specified intervals during the test, followed by spatial clustering of these regions to assess their spatiotemporal evolution. The clustering analysis results demonstrated the extension of existing damage regions was the main damage process during brittle creep, which is consistent with existing models of sub-critical crack growth. In addition, temporal analysis of tensile and shear strains on a point-by-point basis revealed both new damage formation and the strain concentration within existing damaged regions significantly contribute to overall specimen strain during primary creep. In contrast, during secondary creep, increases in specimen deformation are influenced by the accumulation of strains within already damaged regions.

Highlights

- Strain-based evolution of damage is characterized during brittle creep in intact rocks.
- The temporal evolution of tensile and shear strains during primary and secondary creep is quantified.
- Relative influences of newly damaged regions are investigated in evaluating the damage process during creep.

Keywords Stanstead granite · Time-dependent behavior · Brittle creep · Sub-critical crack growth · Spatiotemporal strain evolution

1 Introduction

Increasing the level of applied stresses on brittle rocks results in brittle failure through permanent deformation processes involving microcrack nucleation, growth, interaction, and coalescence (Brace et al. 1966; Bieniawski 1967; Lajtai 1974; Nicksiar and Martin 2012; Hosseini and Tahmasebi 2024). Among the many factors influencing the brittle failure mechanism in rocks such as confining pressure, temperature, and pore pressure, the influence of time is the

✉ Mehrdad Imani
mimanitilenoei@mines.edu

[1] Department of Civil and Environmental Engineering, Colorado School of Mines, Golden, CO 80401, USA

[2] Department of Geology and Geological Engineering, Colorado School of Mines, Golden, CO 80401, USA

[3] Department of Mineral Engineering, New Mexico Institute of Mining and Technology, Socorro, NM 87801, USA

Published online: 26 September 2024

least well-understood (Kranz 1979; Heap 2009; Brantut et al. 2013; Imani et al. 2017; Zhou et al. 2022). Time-dependent behavior in rocks involves the progressive degradation of various mechanical properties over time. Hence, understanding the time-dependent characteristics of brittle rocks is essential for the evaluation of the long-term behavior of rock engineering structures such as underground excavations, rock slopes, nuclear waste repositories, and geothermal systems (Swift and Reddish 2005; Nara et al. 2010; Sone and Zoback 2014; Wang et al. 2021; Zheng et al. 2022). Recently, there has been a notable increase in the evaluation and monitoring of the time-dependent behavior of brittle rocks within engineering applications, such as open-pit mines (Carla et al. 2017; Sun et al. 2023) and underground mining pillars (Hou et al. 2021; Wang et al. 2023), where rocks have low or no confining stress. Brittle creep is one of the well-known time-dependent phenomena describing the inelastic deformation of rocks under constant stress conditions. In other words, in a controlled laboratory setting, the applied stress (below the short-time strength) on a specimen is kept constant, and the strains and deformations are measured as a function of time.

Traditionally, brittle creep has been divided into three distinct stages: (1) Primary (or decelerating) creep, in which the creep strain rate gradually decreases; (2) Secondary (or steady-state) creep, in which the creep strain rate remains approximately constant; (3) Tertiary (or accelerating) creep, in which the creep strain rate increases until the rock fails (Kranz 1979; Baud and Meredith 1997; Zhou et al. 2022; Zafar et al. 2022a). Recent studies have suggested that secondary creep in brittle rocks may not represent a distinct phase, but rather an inflection point between primary and tertiary creep phases. This interpretation is supported by both micromechanical models and experimental observations (Brantut et al. 2012; 2014). However, in practice, variations in strain rate over long periods of time prior to and following the attainment of the inflection point between primary and tertiary creep may be small and relative to the precision of recorded strain measurements, making the identification of a discrete inflection point not possible. In such cases, the time period of approximately constant creep strain rate can be considered as an empirically observable "secondary creep phase", even if such a discrete phase does not fundamentally exist. For the purposes of this study, the delineation between "primary" and "secondary" creep is not intended to represent a fundamental delineation between phases but rather is used to evaluate differences in behavior from the earliest part of creep, where the strain rate decreases by an empirically detectable amount, to a later stage, where the strain rate appears to be approximately constant.

As strain is one of the most important proxies to characterize creep behavior, an in-depth study of time-dependent strain evolution is fundamental to better understand the behavior of rock structures designed for a long period of time (Scholz 1968; Amitrano and Helmstetter 2006; Zhou et al. 2022). Over the past few decades, numerous studies have been performed to investigate brittle creep by evaluation of strain evolution under various loading conditions. Kranz (1979) loaded Barre granite under unconfined compressive stress conditions and evaluated axial and lateral strains during brittle creep. He showed the lateral strain increased faster than the axial strain because of the faster growth of crack width than length or crack coalescence contributing more to the lateral strain. Lockner (1993) assessed the strain rate sensitivity of brittle creep and observed the volumetric strain rate increased with increasing differential stress. Heap et al. (2009; 2011) characterized the brittle creep behavior of sandstone and basalt at various temperatures and under in-situ conditions. In addition to measuring axial strain, they also employed acoustic emission monitoring, and estimated porosity variations as macroscopic indicators to study brittle creep behavior. The axial strain rate was heightened with the increase of applied differential stress, and the accumulated axial strain was shown to be approximately similar before failure regardless of the level of applied stress. Various studies have suggested that time-dependent deformation and damage evolution in brittle rocks occur primarily through sub-critical crack growth, where stress corrosion is the main mechanism behind this phenomenon (Meredith and Atkinson 1983; Atkinson 1984; Amitrano and Helmstetter 2006; Nara et al. 2017; Voigtländer et al. 2018). During sub-critical crack growth, significant crack extension and deformation can occur at the values of the stress intensity factor substantially lower than the critical stress intensity factor, also known as fracture toughness (Atkinson 1984). Consequently, the occurrence of sub-critical crack growth and associated deformation is highly dependent on the environmental and loading conditions such as the presence of chemically active components, temperature, humidity, and stress conditions (Atkinson 1984; Paraskevopoulou et al. 2018). To the best of our knowledge, almost all the available experimental research evaluating and quantifying sub-critical crack growth has been performed using experiments on rock specimens with pre-existing flaws (e.g. Meredith and Atkinson 1985; Nara et al. 2010, 2017; Ko and Kemeny 2013; Voigtländer et al. 2018; Ma et al. 2022). Meredith and Atkinson (1985) used the double torsion test method to study sub-critical crack growth for pre-cracked specimens of Westerly granite and Black gabbro under high-temperature conditions as a corrosive agent and concluded that the elevated temperature led to an increase in the crack growth rate. Nara et al. (2017) used the double torsion test method to study the influence of the surrounding environment on sub-critical crack growth in marble and concluded that the velocity of the crack was higher due to the presence of water compared to air, they also showed that the crack velocity increased

with the increase of relative humidity in air. Voigtländer et al. (2018) carried out a single-edge notch bending creep test on Carrara marble and demonstrated that sub-critical crack growth and inelastic strain accumulation are enhanced by the presence of water.

Accumulation of strains and formation of microcracks eventually result in a macroscopic failure during brittle creep as the failure behavior and rupture of rocks are closely linked to the smaller-scale micro-fracturing process (Kranz 1979; Amitrano and Helmstetter 2006; Brantut et al. 2013). However, it has historically been challenging to determine the link between the time-dependent microscopic fracturing process and the observable macroscopic behavior and rupture. Application of non-destructive test methods has become increasingly popular in the evaluation of rock fracturing processes (Shirole et al. 2020c; Zafar et al. 2022a, b; He et al. 2024). He et al. (2024) evaluated the parameters of the ultrasonic transmitted waves (amplitude, velocity and dominant frequency) to determine crack stress thresholds in different types of rocks. Recent studies utilized AE to evaluate and monitor small-scale cracking and damage processes during brittle creep (Heap et al. 2009; Chu et al. 2022; Zafar et al. 2022a, b). While AE effectively captures the temporal and spatial evolution of the cracking process at small scales, it inherently detects the seismic components of deformation (Renard et al. 2020), and it can be challenging to interpret these observations in the context of specific physical scales. In addition, it does not consider aseismic deformation, which corresponds to more than 99% of accumulated strain (Cartwright-Taylor et al. 2022). Given that sub-critical cracking is known to be a relevant mechanism during brittle creep, where both seismic and aseismic deformation occur, high-resolution strain measurement can provide new insights into creep behavior. Many previous studies have utilized axial, lateral, and volumetric strains to evaluate damage and deformation processes during brittle creep. However, such studies typically consider the global strain accumulation over the entire rock specimen, limiting the degree to which smaller-scale strain evolution processes can be explored. Recently, Digital Image Correlation (DIC) has been increasingly used to study brittle creep behavior (Tal et al. 2016; Zafar et al. 2022a; Traore et al. 2023; Xue et al. 2023; Imani et al. 2023; Shabani et al. 2023). DIC is a well-known technique to compute full-field deformations and strains locally, in contrast to linear variable differential transformers (LVDT) and extensometers measuring global specimen deformation. Zafar et al. (2022a) carried out multistage creep tests using 2D-DIC on double-flawed prismatic Barre granite specimens to evaluate the development of damage and inelastic strains during brittle creep. They quantified the non-elastic portion of strains and showed the non-elastic strains started growing and accumulating from the flaw tips and were consistent with AE signatures. Xue et al. (2023) used 2D-DIC to characterize full-field temporal and spatial strain evolution in single-flawed sandstone specimens during brittle creep experiments. They showed strain accumulation and localization by investigating the effect of different flaw angles on the creep damage process. Traore et al. (2023) employed DIC to evaluate the deformation process during creep behavior in shale and sandstone and showed strain localizations along the lamination boundaries of shale and uniform strain development in the body of sandstone. Li et al. (2021) and Ma et al. (2022) used DIC to study sub-critical crack growth in brittle rocks using double torsion experiments to assess strain evolution and crack propagation processes. Li et al. (2021) showed that the theoretical calculations of sub-critical crack length were consistent with crack length captured by DIC. Ma et al. (2022) used 3D-DIC to evaluate the sub-critical crack growth in basalt and granite and observed the occurrence of sub-critical fracturing in both rocks, but basalt exhibited a faster fracture rate and greater length of sub-critical cracks.

In summary, strain-based analysis has been extensively used to examine brittle creep behavior in both intact rock specimens and those with pre-existing flaws. While many prior studies assessed time-dependent strain evolution on the specimen scale (LVDTs and extensometers), their emphasis typically centered on the monitoring of overall strain evolution. Some studies attempted to address this issue by using the DIC technique, facilitating the investigation of strain accumulation and localization at the grid-point scale; however, a significant research gap exists concerning the temporal and spatial interaction between existing and new damage in rocks during brittle creep. In addition to the limitations in monitoring techniques, most studies have explored brittle creep in rocks with pre-existing cracks by evaluating crack initiation and propagation around the crack tips; however, a comprehensive understanding of the time-dependent interaction and development of distributed and random damage in intact rock specimens has not yet been developed. This study aims to offer insights into the temporal and spatial evolution of non-elastic strains during brittle creep in intact Stanstead granite specimens, using the local strain information at the micro scale by addressing the following research questions: (1) How do newly formed damage features and already existing areas of damage interact and evolve spatially and temporally during creep? (2) What are the relative contributions of local tensile and shear strains to damage evolution during primary and secondary creep? (3) What are the main mechanisms of damage during primary and secondary creep?

To address these questions, the 2D-DIC results were first analyzed to identify the damaged and undamaged grid-points across the surfaces of prismatic rock specimens based on a pixel-scale damage criterion considering both tensile and shear strains. Subsequently, the 2D-DIC grid-points

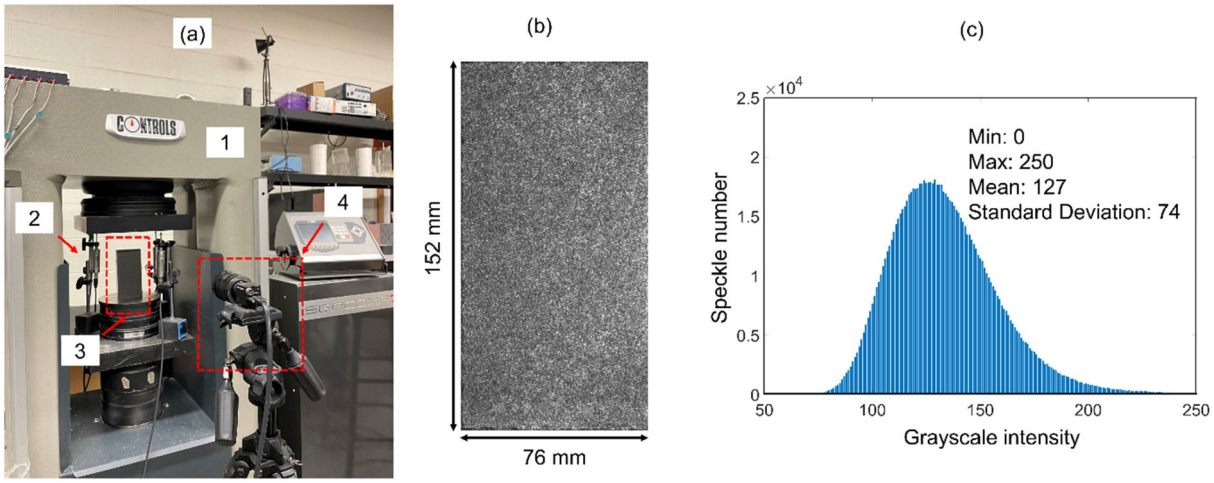

Fig. 1 The experimental setup used to synchronize the evolution of full-field strains captured by 2D-DIC with the various stages of experiment (both monotonic and creep phases), **a-1** loading frame to apply unconfined compression load, **a-2** LVDTs, **a-3** speckled SG specimen, **a-4** CCD camera, **b** speckle pattern on the surface of SG specimen, and **c** grayscale intensity distribution for the surface of speckled SG specimen

were classified for specific time intervals into four distinct categories based on the changes in strain observed: non-damage, strain recovery, existing damage, and new damage. Then, these four distinct categories of grid-points were used to define the three classes of damage obtained by a clustering algorithm. Ultimately, the mechanism of damage was investigated during primary and secondary creep by evaluating the temporal and spatial evolution of damage based on the three introduced classes of damage.

2 Experimental Program

2.1 Material and Testing Procedure

In this study, the intact prismatic Stanstead granite (SG) specimens were used to characterize the damage mechanism during creep experiments. SG is a medium to coarse-grained crystalline rock with typical mineral contents of feldspar (65%), quartz (25%), and biotite (8.5%), and with an average grain size of between 0.5 and 2 mm (Shirole et al. 2020b). The density of the SG specimen is around 2600 kg/m^3 with Young's modulus and poison's ratio of 48 ± 3 GPa and, 0.16 ± 0.02, respectively. A prismatic specimen geometry with dimensions of 152 mm in length, 76 mm in width, and 25 mm in thickness was used for this study. The prismatic shape of specimens has been chosen to ensure a planar surface necessary for accurate in-plane 2D-DIC measurements (Ferrero et al. 2008; Sutton et al. 2009); moreover, a prismatic specimen with a thickness of 25 mm ensures that the stresses perpendicular to the specimen are nearly zero (i.e., plane stress condition) (Musial et al. 2019). In the experimental laboratory, a computer-controlled servo-hydraulic loading machine (Fig. 1a-1) designed by Control Group Inc. was utilized to apply unconfined compression load on the prismatic SG specimens for both monotonic and constant load phases of experiments. The axial loading rate up to the point of constant stress was 550 N/s according to the relevant ISRM suggested method (Fairhurst and Hudson 1999), and the overall axial displacements were measured by three LVDTs that were mounted on the bottom platen of the loading machine to measure the relative movement between the bottom and top platens (Fig. 1a-2).

2.2 2D-Digital Image Correlation (2D-DIC) Setup

Digital image correlation (DIC) is a non-destructive optical method for the computation of full-field deformations and strains of materials. Numerous studies have demonstrated the DIC's ability to provide accurate and consistent results for evaluating the deformation of geomaterials (Ferrero et al. 2008; Tal et al. 2016; Garg et al. 2019; Shirole et al. 2020a; Zafar et al. 2022b; Traore et al. 2023; Xue et al. 2023). The main concept of 2D-DIC is to calculate deformation and strain maps by comparing the reference or undeformed image (the image taken before applying load) with deformed images (the image taken at different sequences of loading). The correlation process involves selecting a reference image that is partitioned into the square of pixels arrays, which is called a "subset". Each subset has a center known as the DIC "grid-point". The subset size indicates the number of pixels in each subset and the distance between these grid-points is referred to as the "step size". For example, in the current work, the values of subset and step size were set to be 15 and 5 pixels,

respectively. 2D-DIC calculates deformations at each grid-point using a displacement-based cross-correlation function applied to subsets distributed across the specimen surface. The calculated displacements at each grid-point create a complete full-field displacement pattern on the specimen surface, which is then spatially analyzed to compute strain tensors across the entire surface at different times as the test progressed. To ensure precise measurement of deformations, each subset must be distinctly identifiable, which is achieved by speckling a high-contrast grayscale distribution as shown in Fig. 1a-3. In this study, to maintain the high quality of the speckle pattern, the rock surface was first cleaned to get rid of any visible contaminants, and then the specimens were painted 2 h before the experiments to ensure the paints adhered effectively according to Shirole et al. (2020a). Furthermore, a grasshopper (point grey) charged coupled device (CCD) camera (Fig. 1a-4) with a 2448 by 2048 square pixel capacity with a Fujinon lens of focal length 35 mm was used to capture images every two seconds during experiments. The camera was set in a parallel position to the normal plane of the specimen and installed at a distance of 900 mm from the specimens to prevent out-of-plane error (Modiriasari et al. 2017). The spatial resolution of DIC was 90 μm/pixel, which means a single pixel has an edge length of 90 μm in the physical space. After the experiments, VIC-2D software was used to compute full-field deformations and strains. Figure 1 shows the loading machine and 2D DIC setup, as well as the speckled specimen and grayscale intensity distribution of pixels.

3 Analysis Method

The initiation and accumulation of damage in rocks are primarily dominated by the tensile damage process (Brace et al. 1966; Stacey 1981; Martin and Chandler 1994; Diederichs et al. 2004; Nicksiar and Martin 2012). The heterogeneous microstructures of rocks can generate local tensile stress concentrations when subjected to external compressive loads, leading to nucleation of local tensile damage within the microstructure of rocks as they are weaker in tension (Diederichs 1999). In addition to tensile damage, shear-induced damage becomes prevalent above the CD level due to the interaction of the tensile strain-induced microcracks (Diederichs et al. 2004; Farahmand and Diederichs 2015). To track the strains associated with tensile and shear damage mechanisms, in this study, both minor principal strain (ε_{22}) and maximum shear strain ($\gamma_{\max} = \frac{\varepsilon_{11}-\varepsilon_{22}}{2}$) were computed from 2D-DIC measurements across the surface of prismatic SG granite specimens. The minor principal strain (ε_{22}) is associated with lateral expansion perpendicular to the direction of uniaxial loading due to Poisson's effect, resulting in a tensile strain field at different stages of the applied load, and maximum shear strain ($\gamma_{\max}$) is used to characterize the occurrence of shear damage (Shirole et al. 2020a; Zafar et al. 2022b). In this context, the term "damage" refers to the onset of non-elastic (inelastic) strains contributing to the formation of microcracks in the body of rocks (Stacey 1981; Eberhardt et al. 1997; Diederichs et al. 2004; Ehsan Ghazvinian 2015; Shirole et al. 2019). The non-elastic components of minor principal strain and maximum shear strain were evaluated based on the determination of the critical tensile strain threshold (ε_c) and critical shear strain threshold (γ_c), obtained by evaluation of different percentiles of the observed shear and tensile strains distributions across the surface of specimens as a function of load (see Shirole et al. (2019), Shirole et al. (2020a), for more information). Shirole et al. (2020a) determined the values of −21e−4 and 35e−4 for non-elastic tensile strain threshold (ε_c), and non-elastic shear strain threshold (γ_c), respectively for Stanstead granite using the same DIC setup as applied in this study. Shirole et al. (2020a) used the non-elastic components of minor principal strain and maximum shear strain to characterize the damage evolution process at various stages of loading in prismatic SG granite specimens under unconfined compression loading and showed that the evolution of non-elastic components of strains were consistent with attenuation of ultrasonic amplitude during experiments. Zafar et al. (2022b) used the same approach to calculate non-elastic components of tensile and shear strains as the indicators of tensile and shear damage to study the time-dependent damage process in prismatic Barre granite specimens with pre-existing flaws. They showed the non-elastic evolution of strains obtained by 2D-DIC were consistent with AE signatures. In current work, these (ε_c) and (γ_c) were determined to be −20e−4 and 36e−4 (for details, please refer to Appendix A), respectively, which are comparable to the findings of Shirole et al. (2020a) and Imani et. al (2023) for the same rock specimens (SG) and same DIC setup.

It is known that rock is a heterogenous material because of different mineral constituents exhibiting varying strength and stiffness at each grain-grain contact; in reality, this is expected to lead to different strain thresholds at which damage occurs. Therefore, applying a constant strain threshold for damage across strain measurements is a simplification adopted by this study. However, this simplification is mitigated by two main factors: (1) the strain values represent average deformation over regions that are larger than the typical grain size, meaning the effective strain threshold for damage at the scale considered will somewhat homogenized; (2) the main mineral constituents in the rock (quartz and feldspar) have similar mechanical characteristics (Sinha and Walton 2020; West and Walton 2023), meaning that the true strain thresholds associated with grains of these minerals and their contacts should be relatively similar.

Identification of the damaged grid-points is the primary objective of this work to study the mechanisms of damage during primary and secondary creep. Existing

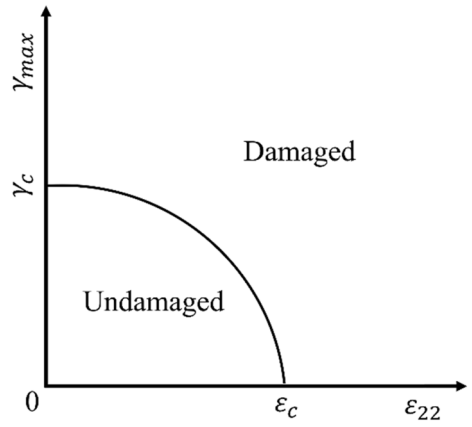

Fig. 2 Schematic graphical representation of damaged and undamaged regions

strain-based criteria that consider the influence of both tensile and shear strains on damage development typically rely on global strain values for damage assessment, and such criteria are therefore not applicable to the smaller-scale strain assessment of this study. As an alternative, we started by considering the damage criterion of Lisjak et al. (2013), who defined damage based on crack opening and slip displacements for evaluation of inelastic failure processes zone to identify mixed mode fracturing. While this criterion was designed for one-dimensional discrete crack elements (based on displacement), the criterion was adopted for application to 2D rock regions (based on strain). Specifically, the damaged grid-points were determined at the pixel scale of SG specimens based on the magnitude of both tensile and shear strains at each grid-point. In other words, instead of considering tensile and shear strains and damage modes separately, we assessed mixed-mode damage according to a modified version of the criterion introduced by Lisjak et al. (2013)

This criterion is defined as follows:

$$\left(\frac{\gamma_{\max,i}}{\gamma_c}\right)^2+\left(\frac{\varepsilon_{22,i}}{\varepsilon_c}\right)^2\geq 1$$

$\gamma_{\max,i}$: maximum shear strain at the i th grid-point, γ_c : non-elastic shear strain threshold, $\varepsilon_{22,i}$: minor principal strain at i th grid-poit, γ_c : non-elastic tensile strain threshold. Figure 2 depicts the visual representation of this criterion between minor principal strain and maximum shear strain. $\left(\frac{\gamma_{\max}}{\gamma_c}\right)$ and $\left(\frac{\varepsilon_{22}}{\varepsilon_c}\right)$ were considered as the ratio of strains at individual grid-point. This figure indicates that those grid-points in the elastic region are considered as "undamaged", and the rest of grid-points that experience non-elastic strains are defined as "damaged".

Prior to applying the criterion, average tensile and shear strain values for each grid-point were calculated using every

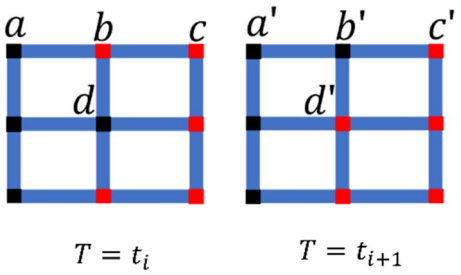

Fig. 3 Schematic representation of damage status at each grid-point (damaged-red and undamaged-black) at time $T = t_i$ and $T = t_{i+1}$

15 images (i.e., every 30 s). This specific averaging interval was chosen to decrease the effects of DIC noise on the results while ensuring that temporal evolution was not compromised. Based on the averaged strain values, the damage criterion was applied to assess all averaged strain maps at various stages of experiment, ultimately classifying each grid-point as "damaged" or "undamaged".

Based on the temporal evolution of this classification, each grid-point was further classified into one of the following four categories over specific time intervals (as defined below): (1) non-damage, (2) strain recovery, (3) existing damage, and (4) new damage.

1. **Non-damage**: grid-points that are classified as "undamaged" at both the beginning and end of the specified interval of interest. The schematic representation in Fig. 3 illustrates a subset of grid-points like those in a typical 2D-DIC, exhibiting the damage status at times t_i and t_{i+1}. In this figure, the damaged and undamaged grid-points are denoted by red and black markers, respectively. For example, according to this figure, both grid-points a (black) and $a\prime$ (black) remain undamaged at both times of $T = t_i$ and $T = t_{i+1}$.
2. **Strain-recovery**: grid-points that are identified as "damaged" at the start of the interval but classified as "undamaged" (within the strain envelope) by the end of the interval of interest. As shown in Fig. 3, the grid-point b (red) is initially recognized as damaged at time $T = t_i$; but it is seen to be undamaged by $T = t_{i+1}$. The strains at this grid-point decrease and revert to the elastic region due to local stress changes or crack closure.
3. **Existing-damage:** grid-points that are classified as "damaged" at both the start and end of the interval of interest. For example, in Fig. 3, the magnitude of strain at grid-point $c\prime$ (red) remains constant or continues to be accumulated by $T = t_{i+1}$ compared to $= t_i$.
4. **New-damage**: grid-points that are classified as "undamaged" at the start of the interval and as "damaged" by the end of interval of interest. For example, as shown in Fig. 3 the grid-point of d' (red) surpasses the damage

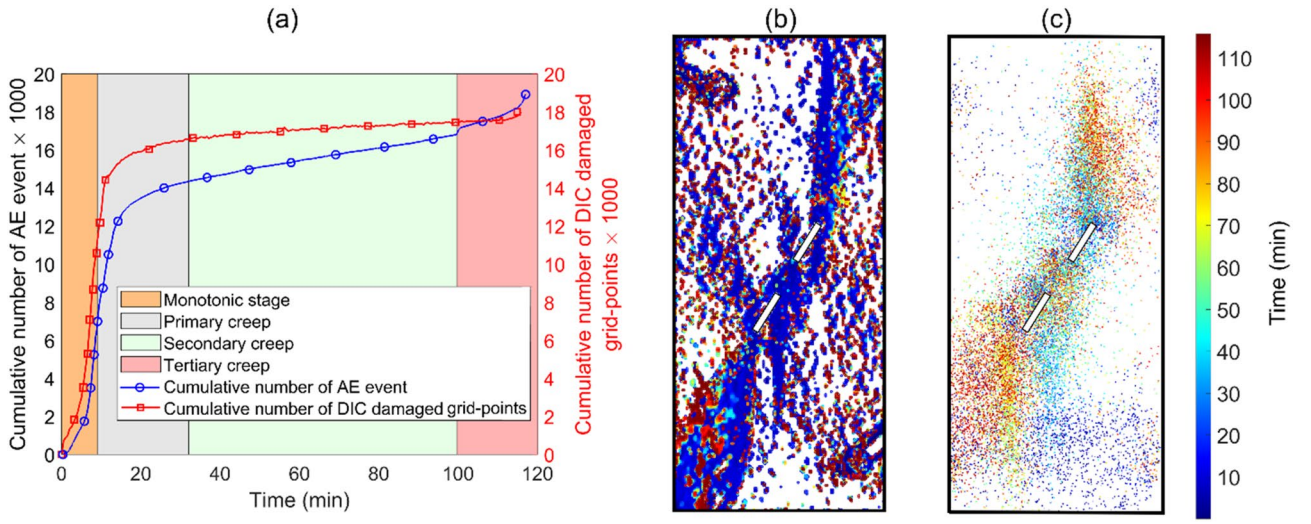

Fig. 4 **a** Cumulative number of AE cracks and DIC damaged grid-points, **b** temporal and spatial evolution of damage captured by DIC during the entire experiment (monotonic and creep), **c** temporal and spatial evolution of damage captured by AE during the entire experiment (monotonic and creep)

threshold at $T = t_{i+1}$ in comparison to the grid-point of d (undamaged) at $T = t_i$.

Before applying the developed method to the intact prismatic SG specimens to assess the interaction between the classified grid-points during the creep phase, this introduced method was initially validated method using data from a prismatic specimen containing two pre-existing flaws (data from Zafar et al. (2023)) to evaluate the method's capability and compared the evolution of non-elastic strains obtained by 2D-DIC with results obtained from AE monitoring (see Sec. 4.1). The main reason for selection of the specimen with pre-existing flaws was microcracking process as they are likely to initiate and grow from the tips of pre-existing flaws, known as stress concentration regions, ultimately leading to the system-size failure of the specimen (Shen 1995; Bobet 2000; Wong and Einstein 2008; Park and Bobet 2009; Yao et al. 2019; Zafar et al. 2022a; Xue et al. 2023). Subsequently, a clustering analysis was conducted to evaluate and damage mechanisms during primary and secondary creep for the tests conducted for this study.

4 Results

4.1 Validation of Analysis Method

This section presents the results of an analysis using the methods described in Sec. 3 applied to a previously published data set, including comparison to AE data as an independent point of comparison (Zafar et al. 2023). Figure 4a shows the cumulative number of DIC damage grid-points and AE events for the entire experiment (monotonic loading and creep phases). This figure demonstrates that the trend in the cumulative number of DIC damaged grid-points is consistent with the cumulative number of AE events. Figure 4b, c present the temporal and spatial evolution of AE events and damaged grid-points obtained by DIC. Both AE and DIC show that the damage localization and evolution started from pre-existing crack tips and then propagated sub-vertically during the entire creep phase and continued into the tertiary creep phase. Note that although general agreement is observed in the trends, one should not expect perfect agreement between the two sets of analyses, as some inelastic strain does occur aseismically, and AE events may occur at some point during inelastic deformation after the initial point of local yield. With all this in mind, the implementation of the introduced analysis method (see Sec. 3) is considered for a double-flawed specimen validated its capability to identify and track damaged regions. Therefore, this approach was applied to intact rocks without pre-existing flaws, where the cracks initiate and grow less systematically.

5 Reference Unconfined Compression Tests

Before the creep experiments, velocity measurements were carried out to select the specimens that exhibited the highest degree of similarity for subsequent experiments. The unconfined compressive strength (UCS) tests were conducted to determine the reference strength and crack damage (CD) threshold of the SG specimens. Five UCS experiments were carried out on the prismatic SG

specimens and the average value of UCS was measured to be 142 MPa with a standard deviation of 5 MPa. The CD threshold was determined as the onset of the softening behavior of the SG specimens obtained by instantaneous tangent modulus (Ghazvinian 2015), and was estimated to be 78% of UCS (111 MPa on average). This obtained CD level corresponds to the average ratio, which is generally consistent with the results from previous research conducted on SG granite specimens (Ghazvinian et al. 2011; Shirole et al. 2020a). Although the Crack Initiation (CI) threshold was not evaluated for these tests, it is known to be approximately 40% of UCS (57 MPa) according to Shirole et al. (2020a) and consistent with previous studies (Nicksiar and Martin 2012; Mutaz et al. 2024).

5.1 Creep Experiments

After the determination of the CD level, creep experiments were carried out on SG specimens. To initiate creep experiments, specimens were loaded up to 110 MPa (approximately equal to the average CD level), and then held constant to initiate creep. The 2D-DIC setup was synchronized with a loading machine to analyze the corresponding images to different stages of creep phases. The entire duration of the creep portion of the experiment was around 5 h because of the limitation in the operation time of loading equipment. The creep experiments were conducted on three SG specimens. All three experiments experienced primary and secondary creep over the length of 5 h. In this section, the results of one test are presented as a representative. Figure 5a shows the stress–strain curve from one of the UCS reference tests. Figure 5b depicts the instantaneous tangent modulus as a function of axial stress for the monotonic loading portion of a creep experiment confirming that the selected SG specimen for the creep test exceeded its CD level (the two other creep-tested SG specimens exceeded the CD level as well). Figure 5c displays the changes in axial strains calculated by 2D-DIC and LVDTs as a function of time during both the monotonic loading (first 6 min) and creep phases of the experiment, exhibiting good agreement between the value of axial strains calculated by LVDTs and 2D-DIC, and demonstrating the effectiveness of 2D-DIC. Figure 5d shows the axial and lateral strains (both calculated by DIC) of the SG specimen for the creep portion of the experiment. Both strain trends demonstrate that the SG specimen experienced primary and secondary creep. The transition point between primary and secondary creep was approximately identified as the point at which the strain rate became approximately constant (see Fig. 5d). The value of lateral strain is higher than axial strain during the creep portion of the experiment. This is because the specimen is loaded above the CD level, meaning significant inelastic lateral dilation occurred during creep, consistent with the findings of Kranz (1979). Both strains and strain rate indicate that the SG specimen did not show any sign of acceleration toward failures (tertiary creep) after 5 h.

5.2 Full-field Strain Maps During Creep

Full-field in-plane strain maps were calculated for minor principal strains and maximum shear strains by image correlation from the start to the end of the test. The computed minor principal strain consists of the positive (contraction) and negative (extensile) values of strains, and grid-points with negative values are representative of tensile strain. Figure 6 illustrates the spatial distribution of ε_{22} and $\gamma_{\max}$ for the start of creep, start of secondary creep, and the end of the test. Figure 6a shows the map of localized tensile strain at the start of creep due to monotonic loading prior to creep (load level equals to ~ 80% of UCS), followed by the continuous evolution of strain during primary and secondary creep as depicted in Fig. 6b, c. The tensile strain maps (Fig. 6a–c) show the development of the subparallel concentration of strain in the direction of axial loading throughout the creep phase, which is associated with the formation of tensile microcracks resulting in lateral expansion. Figure 6e, f demonstrates the spatial distribution of maximum shear strain across the specimen's surface from the beginning of creep to the end of the test and shows that strains had already started to localize by the end of monotonic loading (the beginning of creep) as they had already surpassed the CD threshold at this point. In addition, although prismatic specimens were utilized to evaluate strain evolution, which could potentially lead to stress concentrations and corresponding strain concentrations at the corners of the specimen, Fig. 6 shows that there are no significant strain concentrations near the specimen corners.

5.3 Temporal Evolution of Strains

Visualization of strain maps (Fig. 6) only allows for a qualitative evaluation of strain evolution; however, in this section, the quantification of the non-elastic components of minor principal and maximum shear strains are presented to assess non-elastic strains and damage evolution throughout the experiments. The histograms in Fig. 7 display the strain distributions of DIC grid-points for both minor principal strain (Fig. 7a), and maximum shear strain (Fig. 7b) during creep. The vertical dashed lines in both figures indicate the individual damage thresholds for the tensile and shear strains (−20e−4 and 36e−4, respectively). The histogram results show that DIC grid-point strains were concentrated in the elastic domain considering tensile and shear strains independently; however, as creep progressed, the number of grid-points surpassing

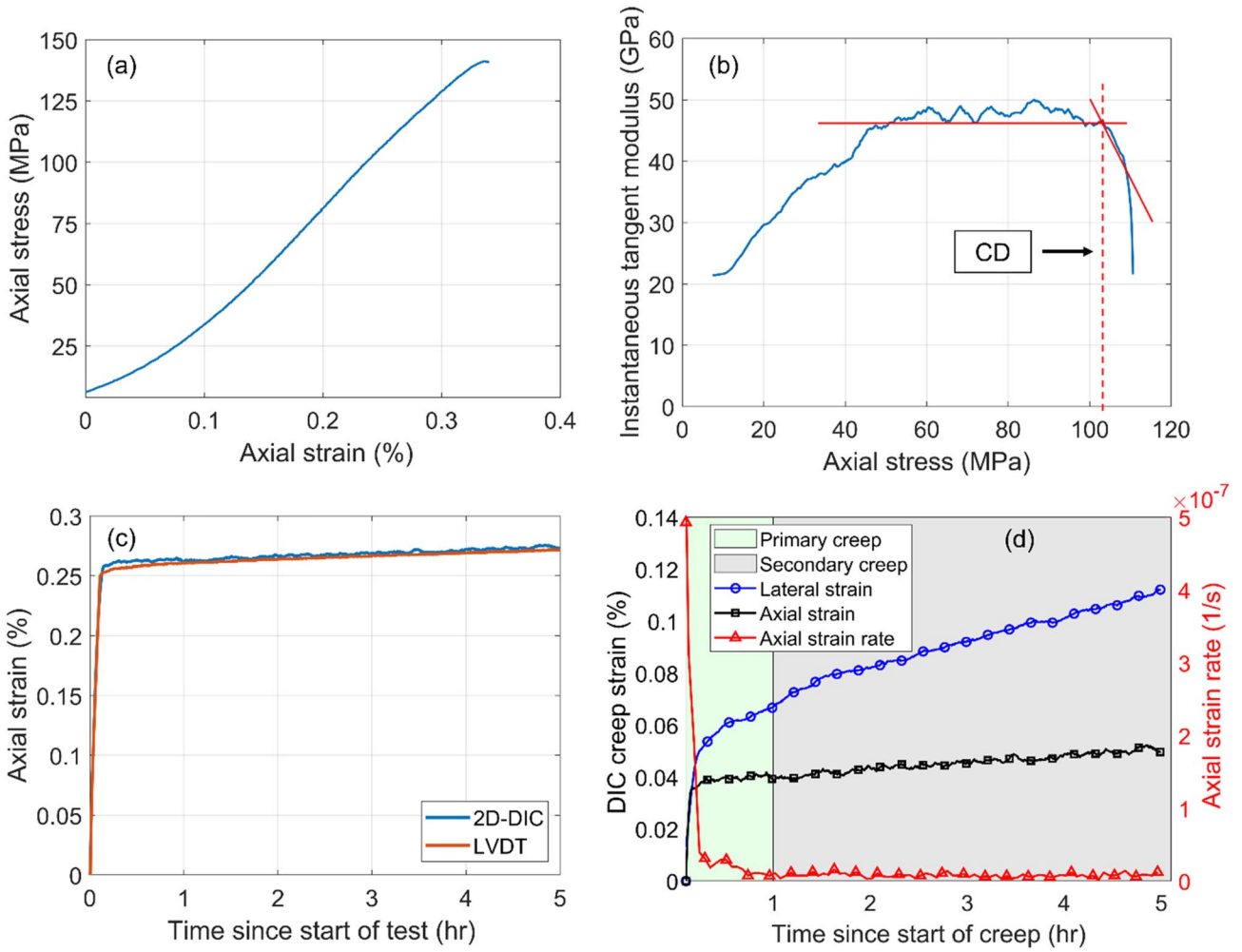

Fig. 5 **a** The stress–strain curve from one of the UCS reference tests, **b** instantaneous tangent modulus graph as a function of axial stress to estimate the CD level, **c** comparison of axial strain calculated by LVDT and 2D-DIC during the entire experiment, **d** variation of DIC creep strains (axial and lateral strains), and axial strain rate during creep portion of the experiment

the individual damage threshold values increased. It is clear that as creep progressed, the strain heterogeneity and localization were increased which means more damage was introduced to specimens over time. Figure 7 illustrates the general temporal evolution of tensile and shear strains; however, it does not provide the accurate identification and precise development of strains at individual grid-points and their contribution to the accumulation of damage. For instance, Fig. 7 is unable to provide information about which grid-points recently crossed the damage threshold, and which ones had already surpassed the threshold and continued to accumulate strain, or even which ones reverted to the elastic region. Therefore, the strain changes were analyzed on a grid-point by grid-point basis. This involved comparing individual grid-points at different time intervals throughout the creep portion of the experiment.

A schematic plot (Fig. 8) was created to illustrate and categorize the different strain regions where the grid-points can be located when comparing two points in time. This schematic plot can be applied to either tensile or shear strains associated with specific critical threshold value (red lines). For example, in Fig. 8, the red solid line is the individual strain component damage threshold (20e−4 and 36e−4) for tensile and shear strain, respectively. The regions can be defined as:

Region (1): elastic strain—grid-points located below the damage threshold for both times of interest.

Region (2): new damage—grid-points that exceeded the damage threshold at the second point in time considered but were below this threshold at the first point in time.

Region (3): strain accumulation—grid-points that exceeded the damage threshold for both times of interest and have accumulated strain from the first point in time to the second (above the 1:1 line).

Region (4): strain loss—grid-points that exceeded the damage threshold for both times of interest, but have a

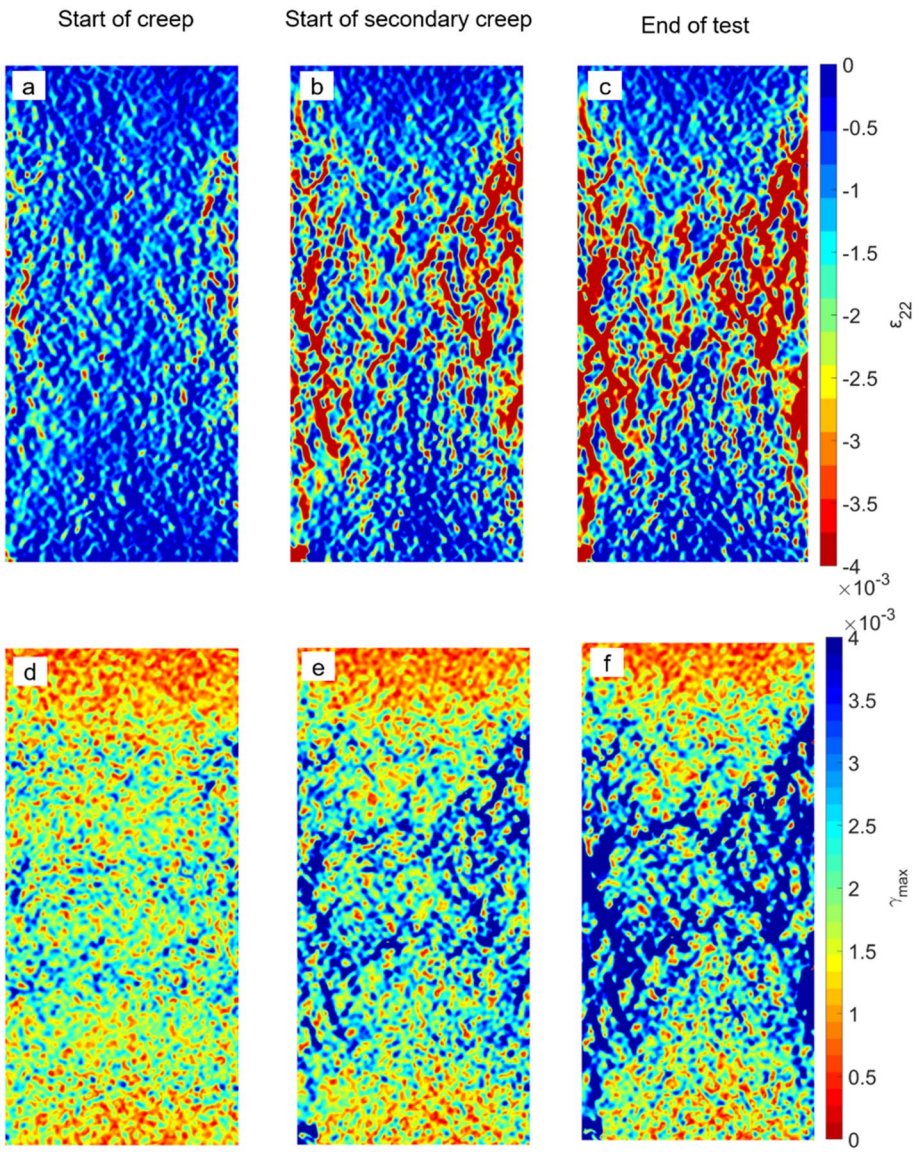

Fig. 6 Spatial distribution of minor principal strain at **a** Start of creep, **b** start of secondary creep, **c** end of test, and spatial distribution of maximum shear strain at **d** start of creep, **e** start of secondary creep, **f** end of test

lower total strain value at the second point in time than the first (below the 1:1 line); this is interpreted to correspond to time-dependent crack closure.

Region (5): recovery of strain to below the damage threshold—grid-points that exceeded the damage threshold at the first point in time but experienced strain recovery to a level that their total strain value falls below the damage threshold at the second point in time.

In this analysis, the evolution of tensile and shear strains was considered for three different time intervals. (1) $t = 6$ min (start of creep) and $t = 1$ h (start of secondary creep), corresponding to primary creep (Fig. 9a, d), (2) $t = 1$ h (start of secondary creep) and $t = 5$ h (end of test), corresponding to secondary creep (Fig. 9b, e), and (3) $t = 6$ min (start of creep) and $t = 5$ h (end of test), corresponding to the entire creep phase of the test (Fig. 9c, f). Figure 9a–f display the tensile and maximum shear strains evolution, respectively, over the three different time intervals. Furthermore, Table 1 provides supplementary quantitative information to aid in the interpretation of Fig. 9 by presenting the percentage of grid-points located within each region.

The temporal evolution of tensile strain at the start of creep is compared with the start of secondary creep in Fig. 9a. The tensile strain contour direction shows the grid-points tended to experience new damage (region 2) and accumulation of strain in existing damaged grid-points (region 3) during primary creep. Table 1 confirms that 1% of grid points were located within region 2 (strain loss) and 8.0% within region 3 (strain accumulation). In Fig. 9b, the tensile strain changes at the end of test were compared with the start of secondary creep. A clear shift in contour direction was evident between primary and secondary creep. According

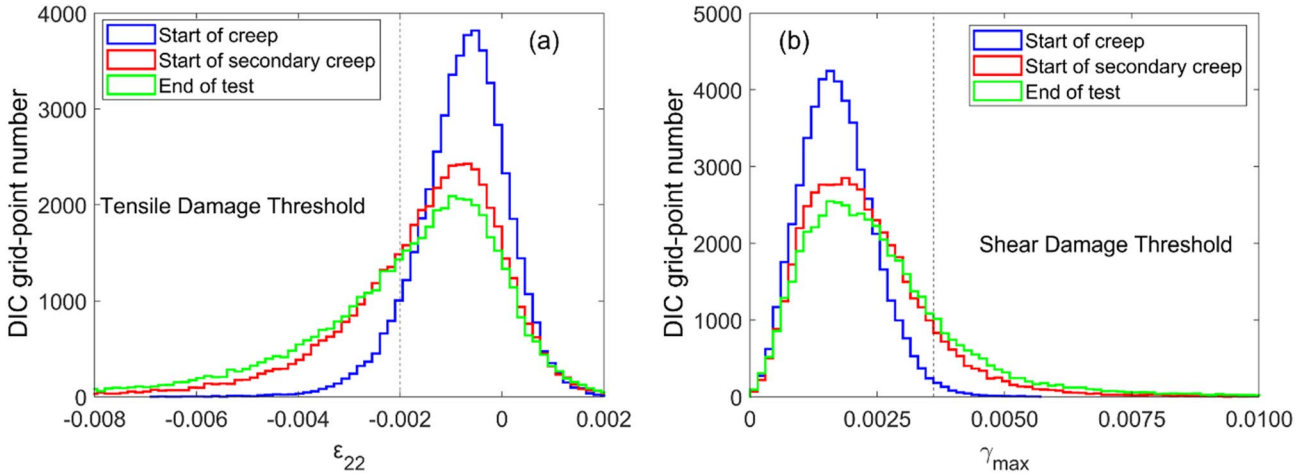

Fig. 7 Comparison of histogram variations at the start of creep, start of secondary creep, and end of test for **a** minor principal strain, **b** maximum shear strain

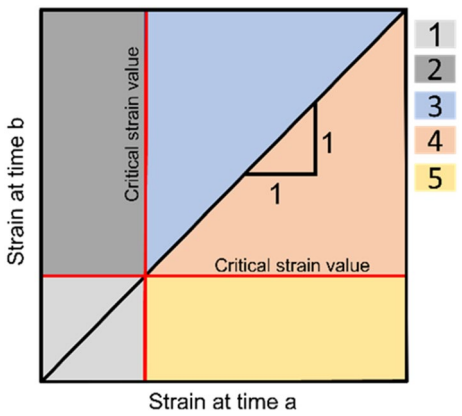

Fig. 8 Schematic plot for temporal evolution of both tensile and shear strains at two different times (time a < time b shows a comparison of an earlier time with a later time) associated with their specific critical threshold value (red lines). Elastic strain (region (1)), New damage (region (2)), Strain accumulation (region (3), above the 1:1 line), Strain loss (region (4), below the 1:1 line), recovery of strain to below the damage threshold (region (5)) (color figure online)

to Table 1, the percentage of grid-points in region 3 (strain accumulation) was higher than in region 2 (strain loss), indicating a greater tendency to accumulate strains and damage in already existing damaged grid-points during secondary creep compared to primary creep. Figure 9d–f displays the same trends for maximum shear strain changes at three different time periods. Given the low percentage of grid-points in regions 4 and 5, strain loss and recovery of strain below the damage threshold showed a negligible impact on the contour plots and apparent mechanisms of strain accumulation during creep. Therefore, Fig. 9 and Table 1 indicate that overall, both the creation of new damage and concentration of strains within existing damaged grid-points significantly contribute to overall specimen deformation and strain during primary creep; during secondary creep, increases in overall specimen deformation are influenced primarily by accumulation of strains within already damaged regions of the specimen.

As discussed in Sec. 3, a mixed-mode criterion was employed considering both tensile and shear strains to distinguish grid-points experiencing either elastic or non-elastic strains at various stages of creep. Figure 10 illustrates the strain values in individual grid-points relative to this criterion at different points during the test, with red points located inside the elastic region ("undamaged grid-points") and the rest of points located in the non-elastic region ("damaged grid-points") shown in blue. According to this figure, the grid-points display a combination of tensile and shear strains indicating distortion and extension occurring simultaneously. However, a significant number of grid-points lie above the 1:1 line, suggesting that despite being mixed-mode in nature, the strain occurring in grid-points exhibiting damage is predominantly extensional in nature. Furthermore, the tendency towards tensile-dominant mixed mode damage is consistent throughout both primary and secondary creep. This DIC-based observation is consistent with earlier studies (Chu et al. 2022; Zafar et al. 2022a; 2023) that concluded brittle creep is a predominantly tensile crack process based on the AE assessment.

The damage assessment procedure depicted visually in Fig. 10 was applied to all the digital images to find the number and locations of damaged grid-points that passed the damage threshold throughout the experiment. Based on this, Fig. 11 shows the cumulative number of grid-points located beyond the damage criterion (non-elastic region). Figure 11 demonstrates that approximately 12,000 grid-points already surpassed the damage threshold at the start of creep; this

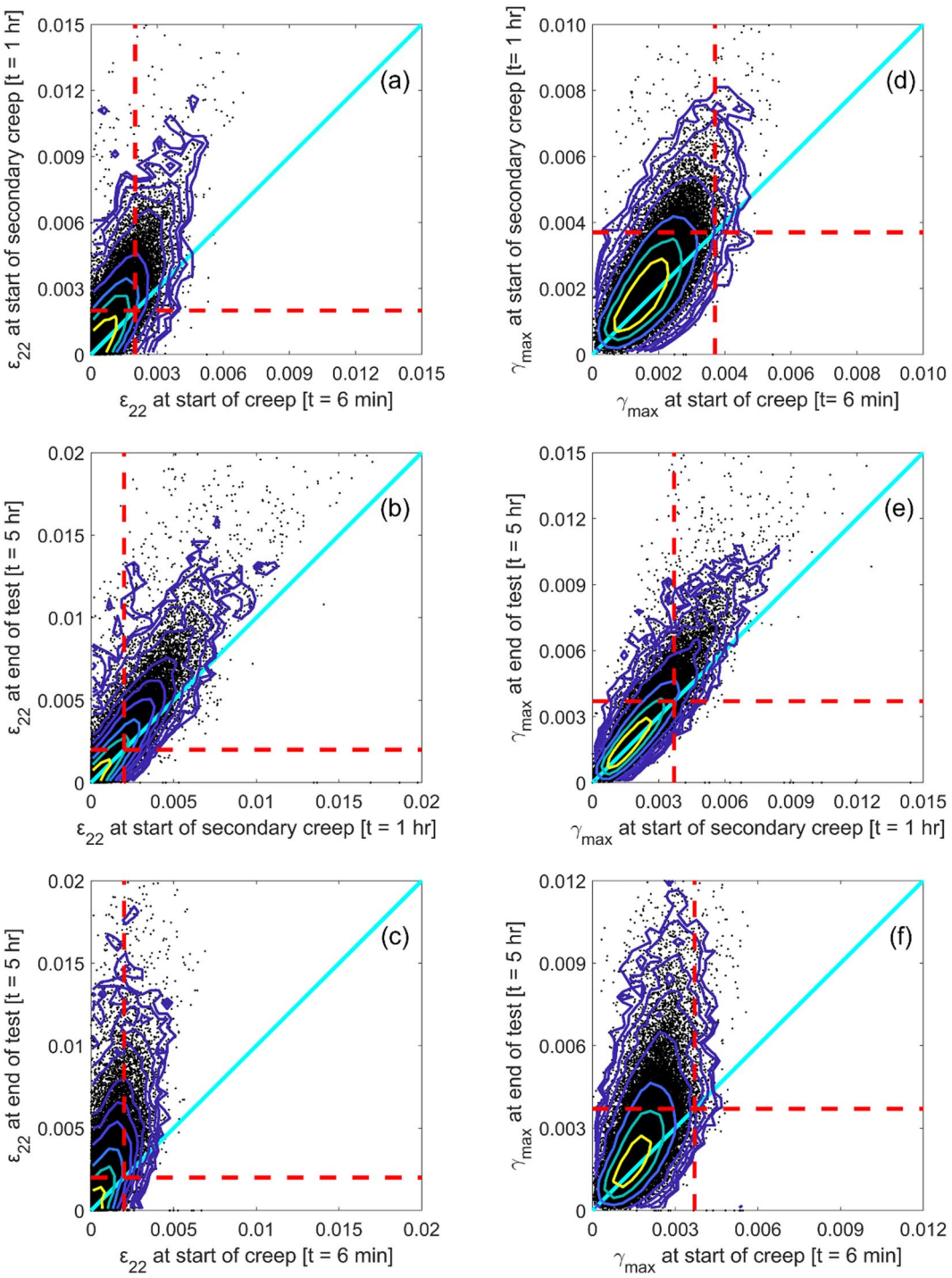

Fig. 9 Contour plots for comparing strains at two different times to evaluate the temporal evolution of both tensile and shear strains. The contours indicate the density of strain grid-points, with colors ranging from dark blue for low density to yellow for high density, **a** comparing tensile strains at start of secondary creep with the start of creep (primary creep), **b** comparing tensile strains at the end of the test with the start of secondary creep (secondary creep), **c** Comparing tensile strains at end of the test with the start of creep (entire creep phase), **d** comparing maximum shear strains at start of secondary creep with the start of creep (primary creep), **e** comparing maximum shear strains at end of the test with the start of secondary creep (secondary creep), **f** comparing maximum shear strains at end of the test with the start of creep (entire creep phase) (color figure online)

Table 1 Percentage of grid-points located in each region (see Fig. 10) for various stages of creep (the numbers rounded to the nearest integer)

Tensile/shear strain	Creep stage	Region 1 (%)	Region 2 (%)	Region 3 (%)	Region 4 (%)	Region 5 (%)
Tensile	Primary creep	71	21	8	0	0
	Secondary creep	59	13	22	4	2
	Entire creep	60	31	7	1	1
Shear	Primary creep	91	8	1	0	0
	Secondary creep	79	9	10	1	1
	Entire creep	83	16	1	0	0

number increased to 19,000 at the beginning of secondary creep and 24,000 at the end of the experiment. Similarly, to the trend observed in the overall axial strain, the number of grid-points exhibiting damage increased at a rapid but decelerating rate during primary creep, followed by a slower (approximately constant) rate during secondary creep.

5.4 Spatial Evolution of Damage

Per Sec. 3, the evolution of the damage status at each grid-point was firstly identified and then categorized over various intervals into four distinct classes: "non-damage", "strain recovery", "existing damage", and "new damage". Figure 12 illustrates the spatial evolution of these categorized grid-points on the intact SG prismatic specimen during primary and secondary creep. As shown in Fig. 12a, the red regions represent the damage that occurred in the SG specimen prior to the start of the primary creep time interval (i.e. due to the monotonic loading of the SG specimen). The green regions in Fig. 12a indicate the grid-points that exhibited damage for the first time during primary creep. Visual examination reveals that many green areas are linked to the red regions, signifying spatial extension of existing damage regions during primary creep. However, some smaller green regions emerged in spatially separate areas, distinct from the pre-existing damage (red regions). The spatial evolution of damage during secondary creep is depicted in Fig. 12b, where red represents all damage that occurred before the start of secondary creep (i.e. during monotonic loading and primary creep) and green represents damage introduced during the 4 h of secondary creep considered.

5.5 Evaluation of Damage Mechanism by the Clustering Algorithm

Figure 12 only considered two relatively long-time intervals. To obtain a better understanding of strain evolution variations occurring during creep and to enhance the resolution of our analysis, the average of strains at each grid-point was computed over intervals spanning every 30 s (with a frame rate of one image every two seconds) from the beginning of monotonic loading to the end of tests. These averaged strains were used to identify the damaged and undamaged grid-points. Subsequently, all these averaged strain maps were sequentially compared over 30-s intervals to classify the grid-points. Following this classification, all grid-points were spatially clustered to evaluate the interaction between existing and new damage over the specified time intervals (30 s) to enhance temporal resolution compared to the longer time intervals as shown in Fig. 12

Density-based spatial clustering of applications with noise (DBSCAN) was applied in MATLAB to grid-points classified as damaged (Ester et al. 1996). The DBSCAN algorithm groups the data points based on their density, distinguishing regions of varying density and recognizing outliers as noise. This algorithm depends on two input parameters: epsilon (maximum radius of the neighborhood) and minimum points. In this study, the minimum point parameter refers to the minimum number of spatially adjacent damaged grid-points required to be considered a cluster, and epsilon is the maximum distance between any two grid-points within a cluster, in units of pixels; these values were set to be two and five, respectively. The choice of five pixels for epsilon corresponds to the minimum distance between two adjacent damaged grid-points (minimum point number) required to identify damaged clusters and regions. In other words, these parameters ensured that all adjacent groups of damaged grid-points would be clustered together. Figure 13 provides an example for a visual illustration of the clustering algorithm applied to the identified damaged grid-points. Figure 13a depicts the spatial distribution of classified grid-points across the surface of the specimen obtained by comparing the two consecutive averaged strain maps over a 30-s interval at the start of primary creep. Figure 13b shows 337 clusters identified by the clustering algorithm, applied to the averaged damaged grid-points in Fig. 13a, and represented by a color based on the size of each cluster (here size means the number of grid-points located within each cluster). The same clustering procedure has been applied to all the averaged strain maps over the specific interval (30 s) during the entire experiment to assess damage mechanisms during creep, and the results are presented in the following sub-sections.

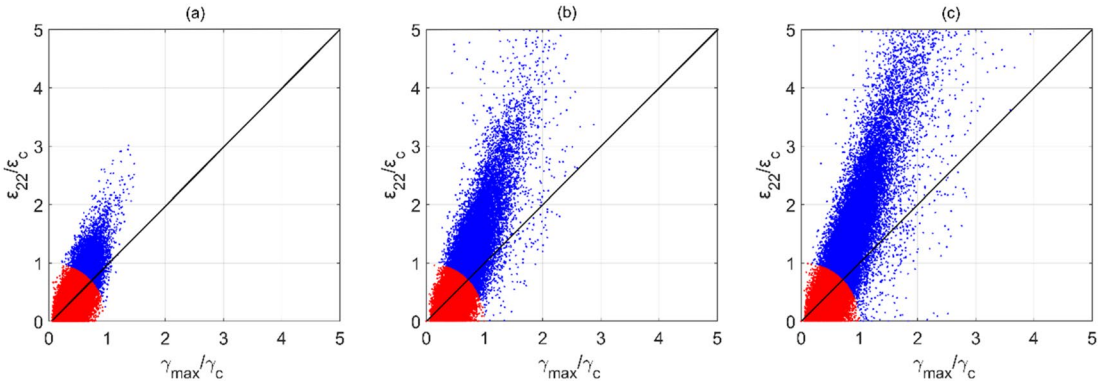

Fig. 10 Presentation of elastic and non-elastic grid-points, red points are the representative of elastic grid-point and blue points are the representative of non-elastic grid-points at, **a** start of creep, **b** start of secondary creep, **c** end of creep test

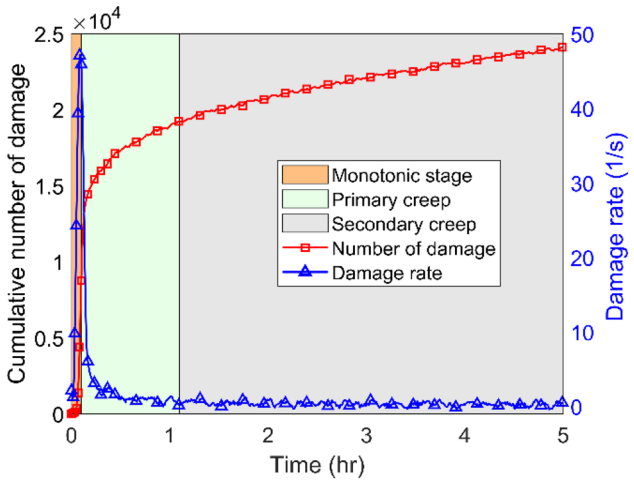

Fig. 11 Cumulative number of damaged grid-points from the start of monotonic load to the end of the test obtained by the coupling criterion introduced in Sec. 3

5.5.1 Number and Size of Clusters

To further evaluate damage mechanisms during creep, all identified clusters were systematically categorized into three distinct classes, each delineated by the types of damaged grid-points (existing and new damage) within. Figure 14 shows a schematic representation of three classes of clusters: (1) clusters containing both existing damage (depicted in red) and new damage (depicted in green), termed as combined damage clusters (Fig. 14a), (2) clusters exclusively composed of existing damage, referred to as isolated existing damage clusters (Fig. 14b), and (3) clusters exclusively composed of new damage, referred to as isolated new damage clusters (Fig. 14c).

Figure 15a illustrates the variations in the numbers of the three types of clusters during the entire experiment. During the monotonic loading stage, the numbers of three categories of clusters increased consistently. Clusters with both existing and new damage tended to be the most prevalent. This trend of combined damage clusters being most common remained during creep, although the absolute number of such clusters tended to decrease rapidly during primary creep, and then more slowly during secondary creep. Based on this, it was hypothesized that many of the clusters merged into bigger clusters during creep, resulting in a reduction in the number of clusters. To evaluate this hypothesis, the emergence of all newly damaged grid-points was examined for the entire duration of the experiment at the specified interval (30 s). Subsequently, the percentage of the new damage grid-points that were situated within combined damage clusters (Fig. 14a) were calculated and compared with those found in isolated new damage clusters (Fig. 14c). Figure 15b shows that the percentage of new damaged grid-points in combined damage clusters exceeds 95%, whereas it is less than 5% in isolated new damage clusters. This observation supports the hypothesis that new damage within the combined damage clusters is responsible for the growth and coalescence of damage during creep, leading to the reduced number of clusters as creep progressed.

Figure 16 depicts the variations of cluster size for three classes of clusters during the entire test. To determine the cluster size, the number of grid-points within each cluster was multiplied by the physical area represented by individual grid-point in the digital image which in this study was 0.2025 mm^2. Figure 16a demonstrates that the total size of the class labeled as "combined damage" occupies a greater portion of the specimen surface compared to other classes. The size of combined damage clusters continuously increased during both the monotonic loading and

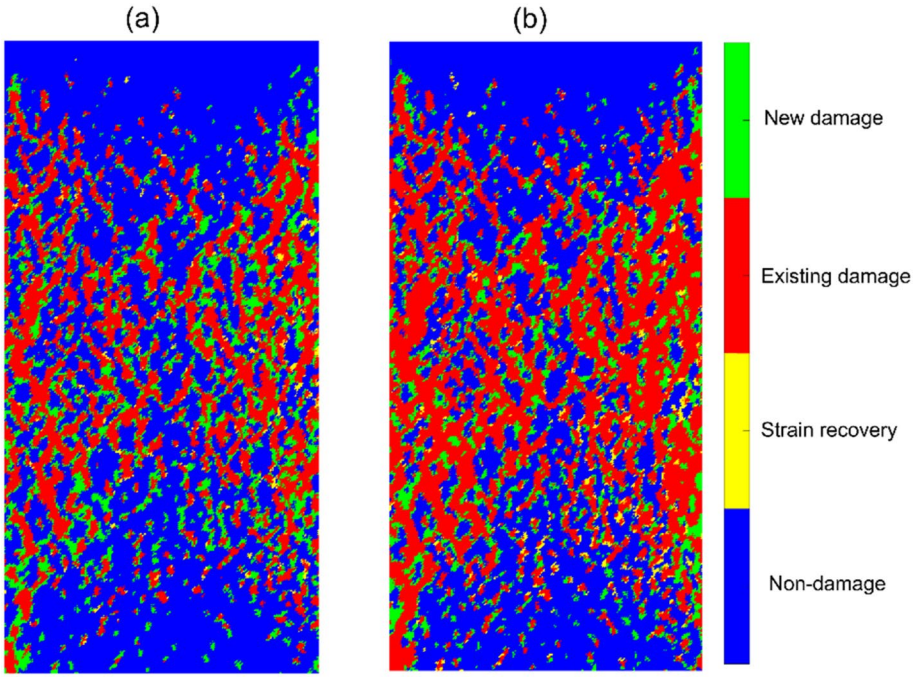

Fig. 12 The spatial evolution of damage in the SG specimen presents by non-damage (blue), strain recovery (yellow), existing damage (red) and new damage (green) across the specimen surface, **a** during primary creep, **b** during secondary creep

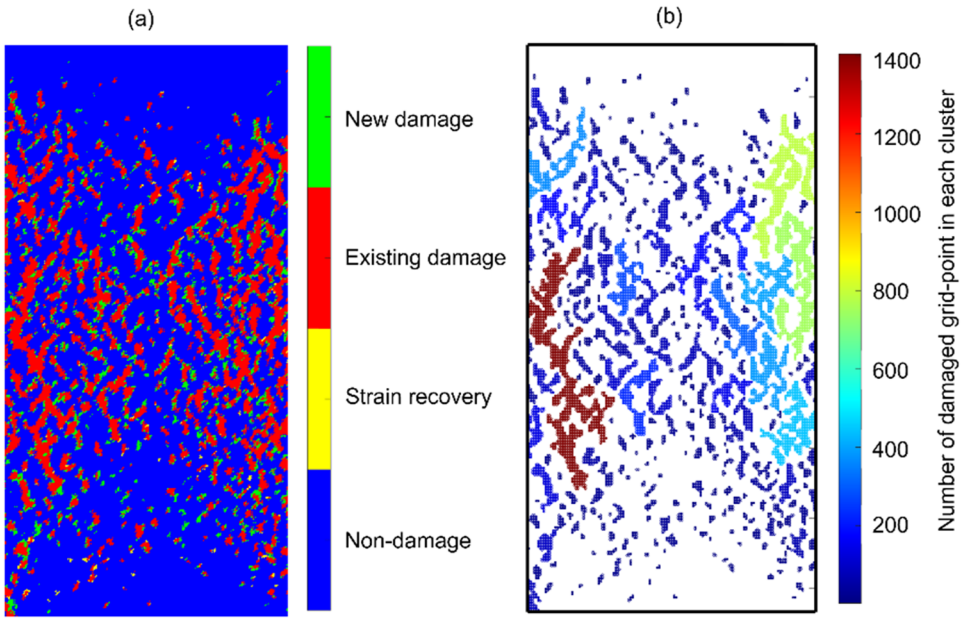

Fig. 13 **a** Spatial distributions of four types of damaged grid-points for the first averaged strain maps at the start of the creep phase, **b** showing 337 identified clusters from DBSCAN based on the number of damaged grid-points inside each cluster

creep phases while the two other ones occupied a small portion of the SG specimen surface. The increasing size of combined damaged clusters is consistent with the merging of combined damage clusters during primary and secondary creep. Figure 16b clearly shows that the area occupied by new damage grid-points in combined damage clusters are greater than those within the isolated new damage regions. Therefore, the new damage that occurred in the combined damaged clusters was mainly responsible for increasing the size of combined damage clusters throughout the creep portion of the experiment. In other words, the new damage areas in combined damage clusters served to spatially connect existing damage. A sensitivity analysis confirm that the interpreted results are generally robust against minor variations in the specific selected tensile

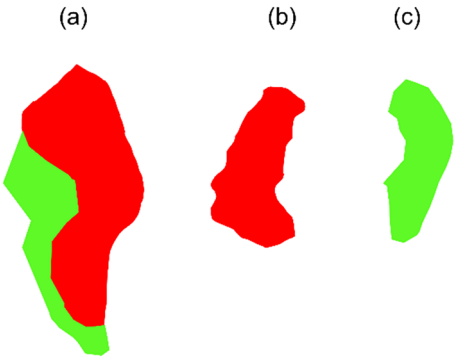

Fig. 14 Schematic presentation of three classes of clusters, **a** cluster named "combined damage" consisting of both new-damage and existing damaged grid-points, **b** Cluster named "isolated existing damage" consisting of only existing damage grid-points, **c** cluster named "isolated new damage" consisting of only new damage grid-points

and shear damage thresholds (see Appendix B for more details)."

5.5.2 Damage Ratio of Clusters

To assess the damage ratio within each cluster, we first calculated a metric refers to as the damage ratio for each grid-point: $\left(\frac{\gamma_{max}/\gamma_c}{\varepsilon_{22}/\varepsilon_c}\right)$. Subsequently, the average damage ratios were separately computed for the three classes of clusters throughout the entire experiment. According to the given function, more relatively tensile damage is observed at smaller values of the damage ratio, while conversely, the emergence of relatively more shear damage corresponds to larger values of the damage ratio. Figure 17 visually presents the spatial evolution of the damage ratio at the start of creep, the start of secondary creep, and the end of the test. These results imply the predominance of tensile damage throughout creep. This evolution manifests through the accumulation of strains in already existing damaged regions and newly formed damage across the specimen surface.

Figure 18 displays the temporal evolution of the computed damage ratio for the three cluster classes from the start of the monotonic loading phase to the end of the test. These results demonstrate that the damage ratio increased consistently during monotonic loading (increased prevalence of shear strains). Following the initiation of creep, however, the damage ratio remained constant and consistent independent of the type of cluster considered; note that the fluctuations in the damage ratio for isolated new damage are due to the small number of clusters consisting of new damage and the small numbers of grid-points included in these clusters. Overall, these results suggest that the relative prevalence of tensile and shear strains that developed during creep was primarily determined by the creep stress; future studies could evaluate this by conducting a similar analysis for tests conducted at a variety of creep stresses.

6 Discussion

6.1 Creep Damage Mechanism

Before evaluating the damage mechanisms associated with the creep experiment, it is required to understand the deformation process and damage mechanisms during the monotonic loading stage. In such experiments, the

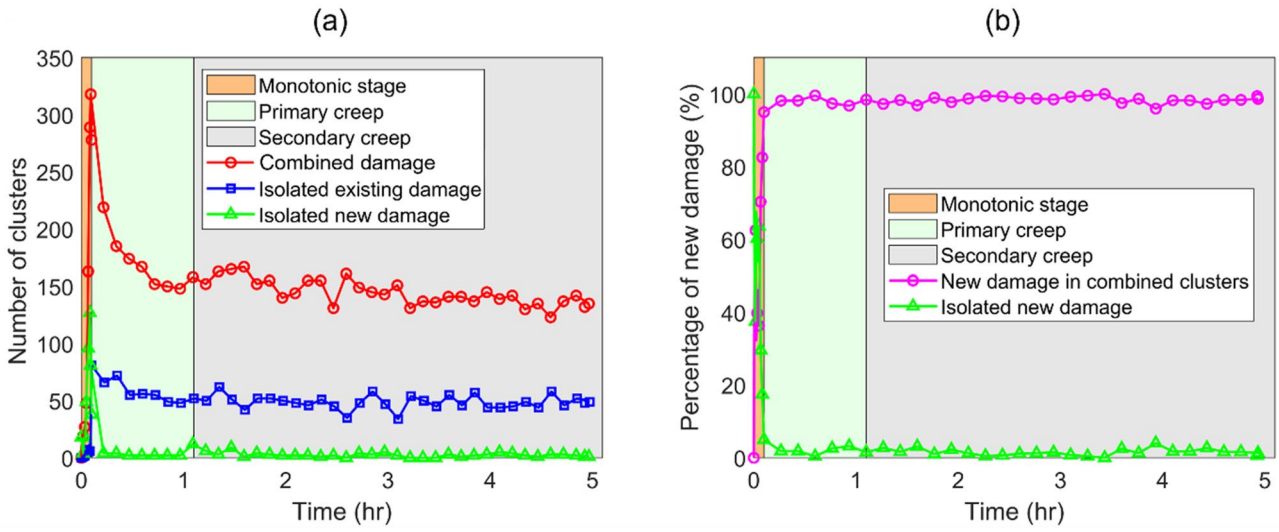

Fig. 15 **a** Shows the variations in the numbers for combined damage, isolated existing damage, and isolated new damage clusters during in monotonic stage, primary creep, and secondary creep, **b** shows the variations in the percentage of new damage grid-points located in combined damage and isolated new damage clusters during the monotonic stage, primary creep, and secondary creep

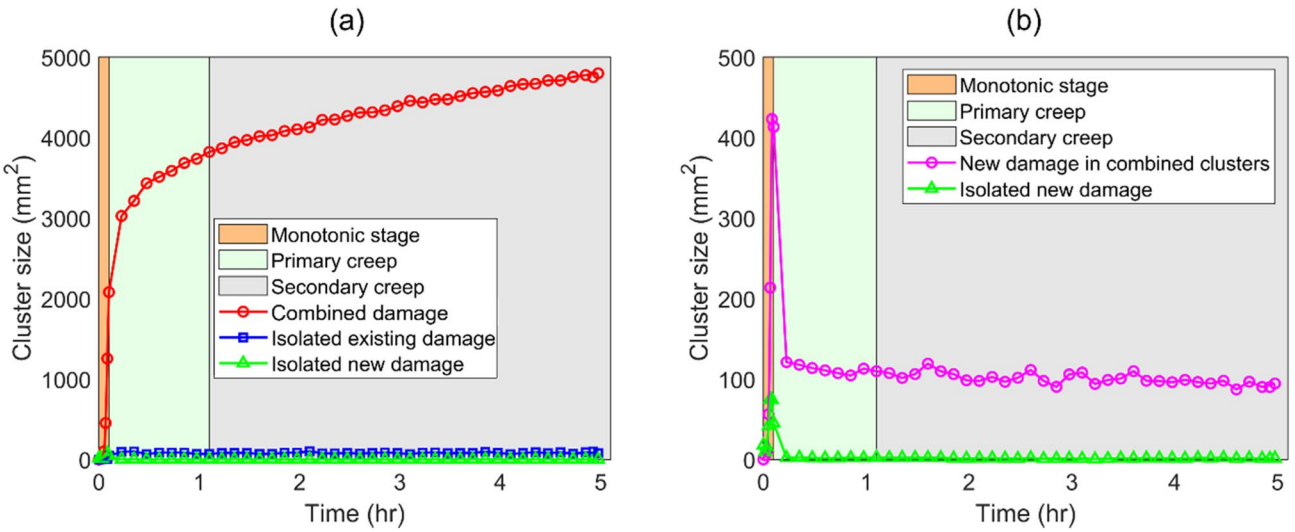

Fig. 16 **a** Shows the variations in the size for combined damage, isolated existing damage, and isolated new damage clusters during in monotonic stage, primary creep, and secondary creep, **b** shows the variations in the occupied cluster size in combined damage and isolated new damage clusters during the monotonic stage, primary creep, and secondary creep

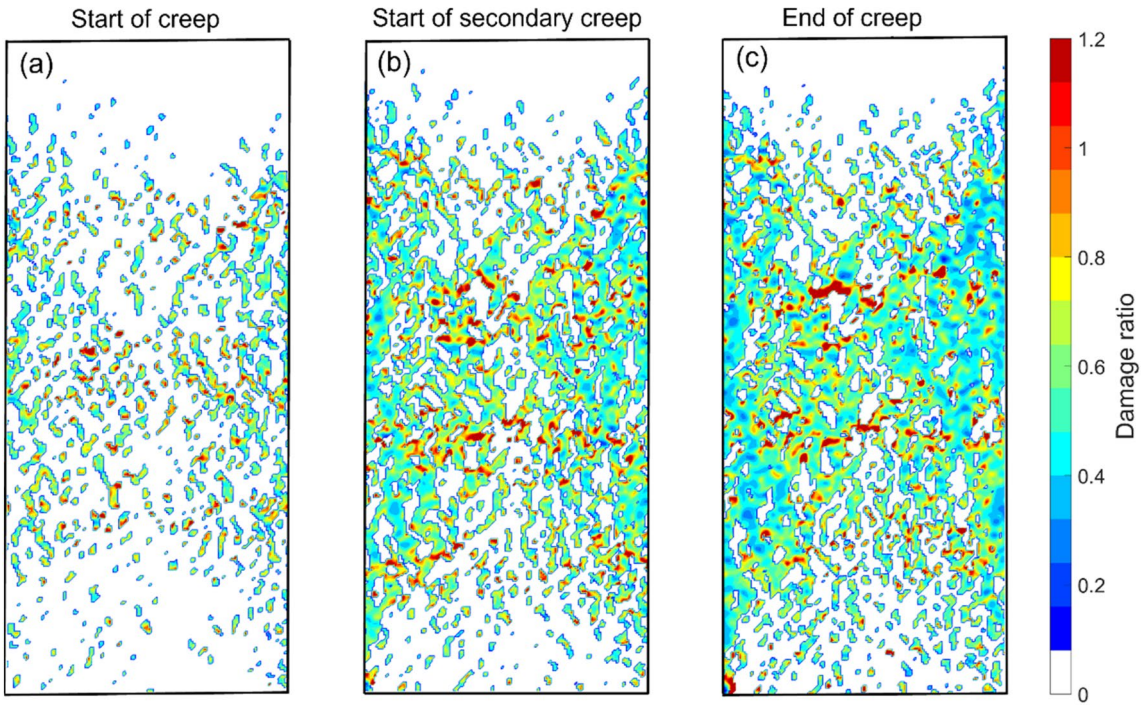

Fig. 17 Spatial distribution of damage ratio at **a** start of creep, **b** start of secondary creep, **c** end of creep (white regions or damage ratio of zero represent non-damage region)

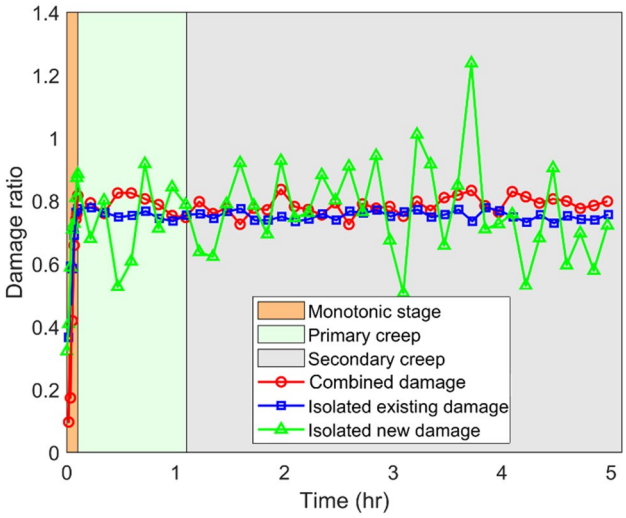

Fig. 18 Shows variations in damage ratio for combined damage, isolated existing damage and isolated new damage clusters during the monotonic stage, primary creep and secondary creep

continuous increase in axial stress leads to the formation of stress-induced cracks. Once the cracks are created, relaxation occurs around the crack tips resulting in local regions of stress drop. As the axial stress continues to increase, the local stresses rise again around the previously formed stress-induced cracks, and this active driving stress tends to increase the length of cracks and create new cracks in the specimen, which are the main mechanism of failure in constant strain rate experiments (Brace et al. 1966; Bieniawski 1967; Kranz and Scholz 1977; Kranz 1979; Lockner 1993; Diederichs 1999; Nicksiar and Martin 2012). Figures 15a and 16a show the number and size of three classes of clusters increased up to the CD level by a concurrent rise in both new and existing damage. This is consistent with the well-understood failure mechanism of brittle rock specimens during the monotonic loading stage as the initiation, interaction, and coalescence of cracks, ultimately lead to a system-scale failure (Brace et al. 1966; Lockner 1993; Eberhardt et al. 1997; Moradian et al. 2016).

On the other hand, under constant stress brittle creep conditions, cracks tend to propagate until the local stress decreases to a sufficiently low level that further growth does not occur (Kranz 1979; Atkinson 1984). Under such conditions, the cracks only continue to grow if the crack tip strength decreases. A primary mechanism by which crack tip strength is understood to decrease is stress corrosion. This phenomenon is responsible for sub-critical crack growth in a stable manner at stress intensity factors below the critical intensity factor, commonly known as fracture toughness. In sub-critical crack growth conditions, the crack propagates until reaching a point where the crack length reaches critical dimensions, leading to dynamic fracture growth and eventual system-scale failure (Scholz 1968; Kranz 1979; Atkinson 1984; Meredith and Atkinson 1985; Brantut et al. 2013). Stress corrosion occurs due to the chemical interactions that take place between chemically active pore fluids, typically water, and strained atomic bonds near crack tips. Diffusion, dissolution, ion exchange, and microplasticity are other mechanisms of sub-critical crack growth that are less common than stress corrosion (Atkinson 1984).

In this study, unconfined compression creep experiments were conducted under room temperature and ambient humidity conditions with the absence of intense corrosive agents that could facilitate sub-critical crack growth. However, even in the absence of such intense corrosive agents, ambient temperature and humidity conditions can still lead to the occurrence of stress corrosion. Specifically, in-room temperature and ambient humidity conditions, the sub-critical crack growth under unconfined stress condition is controlled by a limited fluctuation in temperature and humidity leading to weakening and breakage of atomic bonds at crack tips (Atkinson 1984; Amitrano and Helmstetter 2006). However, the ratio of sub-critical crack length over time can be enhanced by increasing the level of applied stresses (Baud and Meredith 1997; Heap 2009). This is because under higher stress levels, the stress intensity factor is still high and only a small reduction of the strength, caused by stress corrosion, is needed for cracks to propagate. Kranz (1979) showed that increasing applied creep stress on Barre granite under unconfined conditions led to a significant reduction in the time to failure which was further observed by other researchers (Baud and Meredith 1997; Heap 2009; Damjanac and Fairhurst 2010; Paraskevopoulou et al. 2018). In the current study, the SG specimens were loaded up to 80% of UCS to initiate creep under room temperature and ambient humidity conditions. Figure 13a shows spatial introduced damage (red regions) to the SG specimen during the monotonic loading phase. Those red regions are likely to be associated with tensile stress at the tips of the microfractures within damaged regions accelerating the corrosion reaction, and ultimately leading to crack growth and extension of the damaged regions. In addition, the other mechanisms of sub-critical crack growth such as diffusion, dissolution, ion exchange, and microplasticity at crack tips cannot be ruled out.

Kranz (1979) subjected Barre granite specimens to unconfined compression stress at 87% of UCS and subsequently unloaded them at different creep stages to assess the internal structure using a scanning electron microscope (SEM). His findings indicated an increase in both individual crack lengths and crack interactions as creep progressed.

The results of our clustering analysis as depicted in Figs. 15 and 16 extend beyond this finding by demonstrating newly formed damage within the combined damaged regions is responsible for the time-dependent evolution of damage during the creep phase. This illustrates that the newly observed damaged regions not only contribute to the extension of the existing damaged regions but also facilitates the development of interactions between existing damaged regions. Accordingly, the strain-based analysis suggests that the extension of existing damage formed during earlier stages of creep (e.g. by sub-critical cracking) is primarily responsible for damage evolution during brittle creep in the tested specimens. Recent studies (e.g. Ran et al. 2021; Zhao et al. 2020; Zafar et al; 2022a, b) have used AE to study how damage evolves during brittle creep and demonstrated that AE event energy/amplitudes are higher in the early stages of creep, and as creep progresses, lower energy/amplitude events are observed until the onset of tertiary creep, when higher energy/amplitude events are observed again. According to Hellier (2003), the energy/amplitude released from an acoustic emission source is influenced by the speed and size of the event, where sudden cracks emit higher energy/amplitude compared to slow cracks. Therefore, based on Figs. 15 and 16, it is hypothesized that lower energy/amplitude events during secondary creep can be associated with smaller events and slower crack extension and deformation; however, the formation of new isolated cracks or faster crack propagation are associated with higher energy/amplitude and events during primary creep.

6.2 Practical Implications

Our findings can be applied to realistic scenarios under thermo-hydro-mechanical-chemical conditions for brittle creep as the sub-critical crack growth occurs due to the stress corrosion mechanism in all brittle materials. The mechanism of brittle creep is relatively consistent in different scenarios, as loading and environmental conditions can only change the rate and magnitude of the sub-critical crack growth (Atkinson 1987; Baud and Meredith 1997; Brantut et al. 2013; Chu et al. 2022; Heap et al. 2009; Lockner 1993; Sone and Zoback 2014). Therefore, the sub-critical crack growth is expected to be observed in all cases of brittle creep conditions. Accordingly, the implications of our findings have the potential to extend to various large-scale monitoring applications, including open-pit mining projects, rock slopes, debris fans, infrastructure, etc. In all these scenarios, employing similar image processing techniques could allow for a systematic assessment of the evolution of strain and deformation over time. Additionally, the results of our experimental work can be used to calibrate the numerical models to evaluate the long-term behavior of projects under various environmental and loading conditions.

6.3 Limitations and Suggestions for Future Work

In this study, creep experiments were limited to a duration of six hours due to the constraint imposed by the operational time of the loading machine. While the main focus of this investigation was to assess the evolution of non-elastic strain during both primary and secondary creep, future endeavors may aim to extend the experimental duration to days and even weeks using an improved loading apparatus to allow for observation of tertiary creep. In the current study, creep experiments were conducted under unconfined compressive loading conditions at room temperature and in an ambient humidity environment. Although we believe that our research findings would be comparable across diverse loading and environmental conditions as long as the failure is brittle; to comprehensively characterize deformation and strain under varying circumstances, future investigations could consider creep experiments under different loading (e.g. triaxial and true triaxial) and environmental conditions. With regards to the application of 2D-DIC, while the surface deformation and strain are representative of internal structure changes of the specimen for this specific prismatic geometry, other tools such as active ultrasonic monitoring can be applied in future work to evaluate internal damage and stiffness changes for comparison with 2D-DIC results.

7 Conclusions

There have been limited research studies on how time-dependent small-scale damage evolves temporally and spatially in intact brittle rocks where the distributed damage can interact and coalesce during creep. This study presented the results of unconfined compressive creep tests on SG specimens loaded up just above the crack damage threshold (~ 80% of UCS) before the initiation of creep. In this work, 2D-DIC was utilized to monitor the spatial–temporal strain evolution during creep by computing tensile and maximum shear strain profiles. To assess the evolution of damage, the non-elastic components of tensile strain and maximum shear strain were calculated to define the damaged grid-points across the SG specimen surface.

Temporal analysis of strain during creep showed the deformation and strain in the specimens results from the formation of new damaged regions and strain concentrations during primary creep, along with the further accumulation of strains in already damaged regions during secondary creep. Grid-points determined to contain damage were initially identified and subsequently classified into four

categories: non-damage, strain recovery, new damage, and existing damage. This classification aimed to examine the spatial evolution of damage. To investigate the interaction, coalescence, and development of damaged grid-points during creep, a clustering algorithm was applied to all damaged grid-points, resulting in the identification of three types of clusters: combined new and existing damage, isolated existing damage, and isolated new damage. These three classes were evaluated based on their variations in number, size, and strains throughout the creep experiment. The number of combined new and existing damage clusters decreased, whereas their size increased during creep, leading to the merging of existing damage. The presence of new damage in combined existing and new damage clusters was responsible for connecting and sub-critically extending regions of existing damage. Ultimately, this study was the first strain-based analysis to demonstrate that the extension of existing damage is the main mechanism of damage during brittle creep in intact rock, whereas the appearance of new isolated regions of damage plays a minor role in the overall specimen damage mechanism.

Appendix A

As discussed in Sec. 3, the non-elastic components of minor principal strain and maximum shear strain were evaluated by determining the critical tensile strain threshold (ε_c) and critical shear strain threshold (γ_c). These thresholds were identified by analyzing different percentiles of the observed shear and tensile strain distributions across the specimen's surface as a function of load (see Shirole et al. (2019) and Shirole et al. (2020a) for justification of this approach). It is well-known that tensile crack accumulation accelerates after the CI threshold, with only a few tensile cracks expected to form before reaching this point (Eberhardt et al. 1997; Diederichs et al. 2004). The ε_{22} distribution analysis revealed that the 2nd percentile of strain significantly increases after CI, indicating tensile damage progression. Consequently, as shown in Fig. 19a, the 2nd percentile of ε_{22} at CI was selected as the critical tensile strain limit ($\varepsilon_c = -20e{-}4$). Furthermore, shear-induced damage becomes prevalent above the CD level due to the interaction of the tensile strain-induced microcracks (Diederichs et al. 2004; Farahmand and Diederichs 2015). As shown in Fig. 19b, the 0.5th percentile of strain shows a distinct deviation from linearity at the CD stress threshold, indicating the onset of significant shear damage. This point of deviation from linearity was used to estimate the critical shear strain limit ($\gamma_c = 36e{-}4$).

Appendix B

In this study, as mentioned in Sec. 3, tensile and shear damage thresholds were used for the mixed-mode criterion to assess damage at each grid-point. To evaluate the reliability of the results, the damage thresholds were adjusted by $\pm 10\%$ ($\varepsilon_c = -18e{-}4, -20e{-}4, -22e{-}4$ and $\gamma_c = 32.4e{-}4, 36e{-}4, 39.6e{-}4$) to observe their effect on the results and interpretations. Accordingly, Figs. 15 and 16 were reproduced using these adjusted values. As shown in Figs. 20, 21, 22, 23, the results confirmed that changing the damage thresholds did not affect the overall interpretations of this study, as the primary fracturing mechanism remained the extension of already damaged regions, consistent with subcritical crack growth during brittle creep.

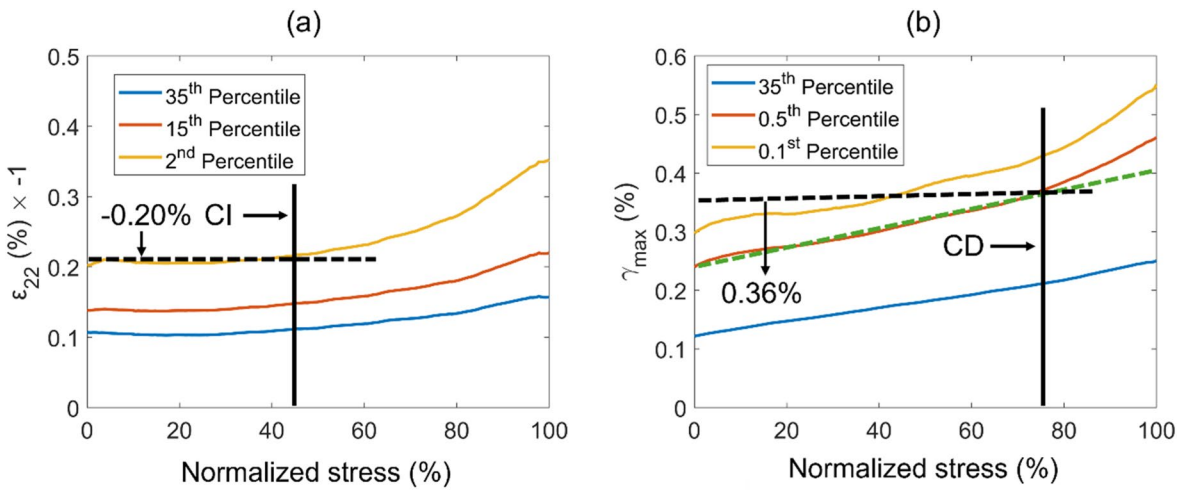

Fig. 19 **a** Evaluation of tensile damage threshold at pixel scale, **b** evaluation of shear damage threshold at pixel scale

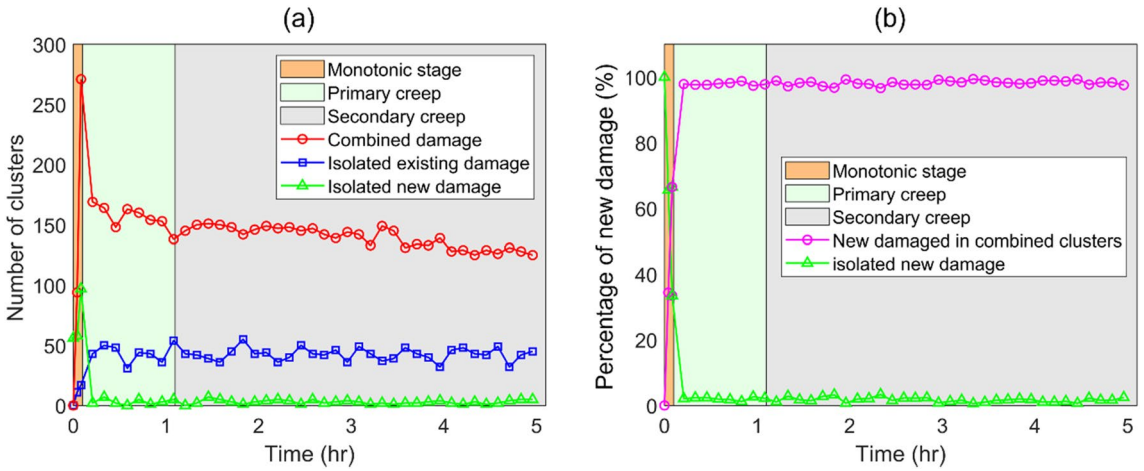

Fig. 20 **a** The variations in the numbers for combined damage, isolated existing damage, and isolated new damage clusters during in monotonic stage, primary creep, and secondary creep for the damage thresholds 10% lower than those used in the manuscript, **b** the variations in the percentage of new damage grid-points located in combined damage and isolated new damage clusters during the monotonic stage, primary creep, and secondary creep for the damage thresholds 10% lower than those used in the main analysis

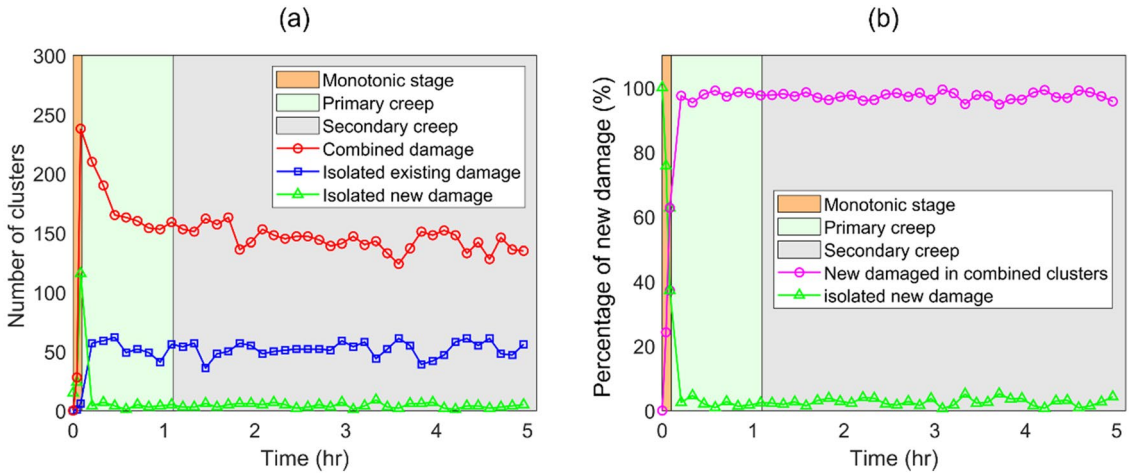

Fig. 21 **a** The variations in the numbers for combined damage, isolated existing damage, and isolated new damage clusters during in monotonic stage, primary creep, and secondary creep for the damage thresholds 10% higher than those used in the manuscript, **b** the variations in the percentage of new damage grid-points located in combined damage and isolated new damage clusters during the monotonic stage, primary creep, and secondary creep for the damage thresholds 10% higher than those used in the main analysis

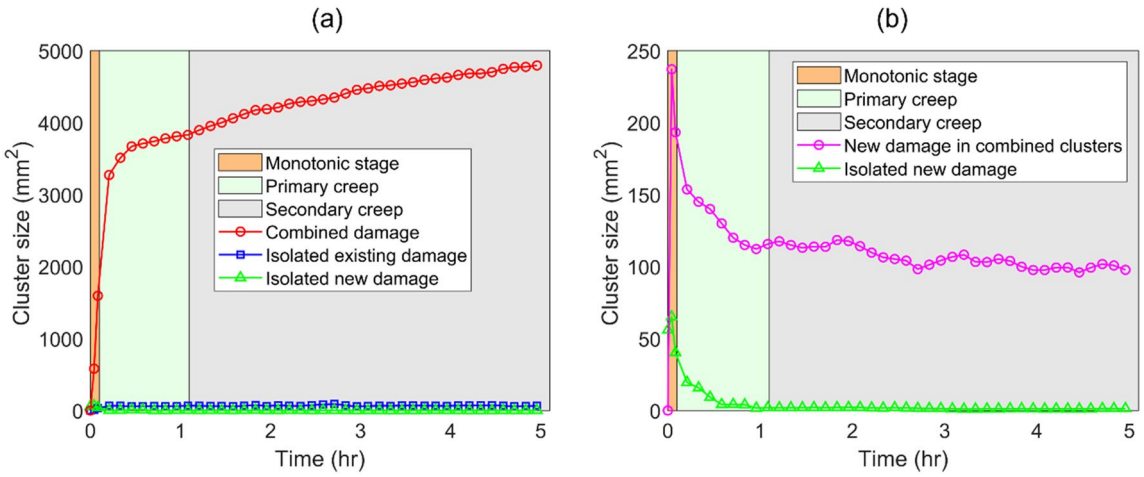

Fig. 22 **a** The variations in the size for combined damage, isolated existing damage, and isolated new damage clusters during in monotonic stage, primary creep, and secondary creep for the damage thresholds 10% lower than those used in the manuscript, **b** the variations in the occupied cluster size in combined damage and isolated new damage clusters during the monotonic stage, primary creep, and secondary creep for the damage thresholds 10% lower than those used in the main analysis

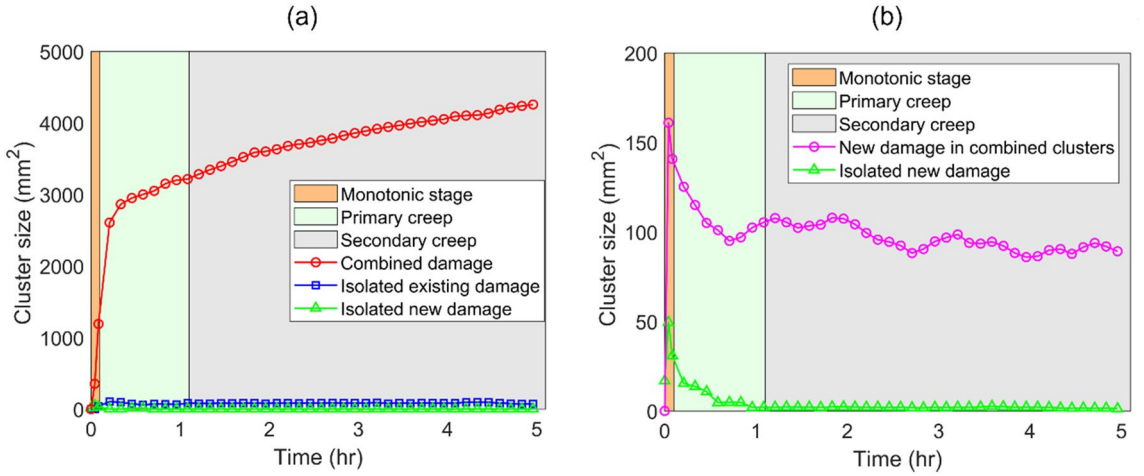

Fig. 23 **a** The variations in the size for combined damage, isolated existing damage, and isolated new damage clusters during in monotonic stage, primary creep, and secondary creep for the damage thresholds 10% higher than those used in the manuscript, **b** the variations in the occupied cluster size in combined damage and isolated new damage clusters during the monotonic stage, primary creep, and secondary creep for the damage thresholds 10% higher than those used in the main analysis

Acknowledgements This research article is based upon the work supported by the U.S. Department of Energy, Office of Basic Energy Sciences, under Award Number DE-SC0019117. This support is gratefully acknowledged.

Funding U.S. Department of Energy, Office of Basic Energy Sciences, DE-SC0019117, Ahmadreza Hedayat.

Data availability The data that support the findings of this study are available upon request from the corresponding author [Mehrdad Imani].

Declarations

Conflict of interest The authors declare that they have no competing financial interests or personal relationships that could have appeared to influence the work reported in this paper.

References

Amitrano D, Helmstetter A (2006) Brittle creep, damage, and time to failure in rocks. J Geophys Res Solid Earth 111:11201. https://doi.org/10.1029/2005JB004252

Atkinson BK (1984) Subcritical crack growth in geological materials. J Geophys Res Solid Earth 89(B6):4077–4114. https://doi.org/10.1029/JB089iB06p04077

Atkinson BK (1987) Fracture mechanics of rock. Academic Press, Cambridge

Baud P, Meredith PG (1997) Damage accumulation during triaxial creep of Darley Dale sandstone from pore volumetry and acoustic emission. Int J Rock Mech Min Sci 34(3–4):24-e1. https://doi.org/10.1016/S1365-1609(97)00060-9

Bieniawski ZT (1967) Mechanism of brittle fracture of rock: part I—theory of the fracture process. Int J Rock Mech Min Sci Geo Abs 4:395–406. https://doi.org/10.1016/0148-9062(67)90030-7

Bobet A (2000) The initiation of secondary cracks in compression. Eng Fract Mech 66:187–219. https://doi.org/10.1016/S0013-7944(00)00009-6

Brace WF, Paulding BW, Scholz C (1966) Dilatancy in the fracture of crystalline rocks. J Geophys Res 71:3939–3953. https://doi.org/10.1029/JZ071i016p03939

Brantut N, Baud P, Heap MJ, Meredith PG (2012) Micromechanics of brittle creep in rocks. J Geophys Res Solid Earth. https://doi.org/10.1029/2012JB009299

Brantut N, Heap MJ, Meredith PG, Baud P (2013) Time-dependent cracking and brittle creep in crustal rocks: a review. J Struct Geol 52:17–43. https://doi.org/10.1016/j.jsg.2013.03.007

Brantut N, Heap MJ, Baud P, Meredith PG (2014) Mechanisms of time-dependent deformation in porous limestone. J Geophys Res Solid Earth 119(7):5444–5463. https://doi.org/10.1002/2014JB011186

Carlà T, Farina P, Intrieri E, Botsialas K, Casagli N (2017) On the monitoring and early-warning of brittle slope failures in hard rock masses: examples from an open-pit mine. Eng Geol 228:71–81. https://doi.org/10.1016/j.enggeo.2017.08.007

Cartwright-Taylor A, Mangriotis MD, Main IG, Butler IB, Fusseis F, Ling M, Magdysyuk OV (2022) Seismic events miss important kinematically governed grain scale mechanisms during shear failure of porous rock. Nat Commun 13(1):6169. https://doi.org/10.1038/s41467-022-33855-z

Chu Z, Wu Z, Wang Z (2022) Micro-mechanism of brittle creep in saturated sandstone and its mechanical behavior after creep damage. Int J Rock Mech Min Sci 149:104994. https://doi.org/10.1016/j.ijrmms.2021.104994

Damjanac B, Fairhurst C (2010) Evidence for a long-term strength threshold in crystalline rock. Rock Mech Rock Eng 43:513–531. https://doi.org/10.1007/s00603-010-0090-9

Diederichs MS (1999) Instability of hard rockmasses, the role of tensile damage and relaxation. University of Waterloo, Waterloo (**Dissertation**)

Diederichs MS, Kaiser PK, Eberhardt E (2004) Damage initiation and propagation in hard rock during tunnelling and the influence of near-face stress rotation. Int J Rock Mech Min Sci 41(5):785–81. https://doi.org/10.1016/j.ijrmms.2004.02.003

Eberhardt E, Stead D, Stimpson B, Read RS (1997) Changes in acoustic event properties with progressive fracture damage. Int J Rock Mech Min Sci 34(3–4):71-e1. https://doi.org/10.1016/S1365-1609(97)00062-2

Ester M, Kriegel HP, Sander J, Xu X (1996) A density-based algorithm for discovering clusters in large spatial databases with noise. In: KDD'96: proceedings of the second international conference on knowledge discovery and data mining, 96(34) 226–231

Fairhurst C, Hudson J (1999) Draft ISRM suggested method for the complete stress-strain curve for intact rock in uniaxial compression. Int J Rock Mech Min Sci 36(3):279–28

Farahmand K, Diederichs MS (2015) A calibrated synthetic rock mass (SRM) Model for simulating crack growth in granitic rock considering grain scale heterogeneity of polycrystalline rock. In: ARMA US rock mechanics/geomechanics symposium. pp. ARMA-2015

Ferrero AM, Migliazza M, Roncella R, Tebaldi G (2008) Analysis of the failure mechanisms of a weak rock through photogrammetrical measurements by 2D and 3D visions. Eng Fract Mech 75:652–663. https://doi.org/10.1016/j.engfracmech.2007.03.041

Garg P, Hedayat A, Griffiths D V (2019) Coupled ultrasonic and digital imaging of crack initiation and growth in prismatic lyon sandstone rocks. In: ARMA US rock mechanics/geomechanics symposium. pp. ARMA-2019

Ghazvinian E (2015) Fracture initiation and propagation in low porosity crystalline rocks: implications for excavation damage zone (EDZ) mechanics. Queen's University, Kingston (**Dissertation**)

Ghazvinian E, Diederichs M, Archibald J (2011) Challenges related to standardized detection of crack initiation thresholds for lower-bound or ultra-long-term strength prediction of rock. In: Pan-Am CGS geotechnical conference

He J, Serati M, Veidt M, De Alwis A (2024) Determining rock crack stress thresholds using ultrasonic through-transmission measurements. Inte J Coal Sci Technol 11(1):19. https://doi.org/10.1007/s40789-024-00669-x

Heap MJ (2009) Creep: time-dependent brittle deformation in rocks. University College London, London (**Dissertation**)

Heap MJ, Baud P, Meredith PG (2009) Influence of temperature on brittle creep in sandstones. Geophys Res Lett. https://doi.org/10.1029/2009GL039373

Heap MJ, Baud P, Meredith PG (2011) Brittle creep in basalt and its application to time-dependent volcano deformation. Earth Planet Sci Lett 307:71–82. https://doi.org/10.1016/j.epsl.2011.04.035

Hellier C (2003) Handbook of nondestructive evaluation (No. 19496). Mcgraw-hill, New York

Hosseini MA, Tahmasebi P (2024) A novel graph-based 3D breakage method for angular particles with an image-based DEM. Int J Rock Mech Min 174:105640. https://doi.org/10.1016/j.ijrmms.2024.105640

Hou R, Xu L, Zhang D, Shi Y, Shi L (2021) Experimental investigations on creep behavior of coal under combined compression and shear loading. Geofluids 2021:1–11. https://doi.org/10.1155/2021/9965228

Imani M, Nejati HR, Goshtasbi K (2017) Dynamic response and failure mechanism of Brazilian disk specimens at high strain rate. Soil Dyn and Earthq Eng 100:261–269. https://doi.org/10.1016/j.soildyn.2017.06.007

Imani M, Walton G, Moradian O, Hedayat A (2023) Monitoring of primary and secondary creep in granite using ultrasonic monitoring and digital image correlation. In: ARMA US rock mechanics/geomechanics symposium. pp. ARMA-2023

Ko TY, Kemeny J (2013) Determination of the subcritical crack growth parameters in rocks using the constant stress-rate test. Int J Rock Mech Min Sci 59:166–178. https://doi.org/10.1016/j.ijrmms.2012.11.006

Kranz RL (1979) Crack growth and development during creep of Barre granite. Int J Rock Mech Min Sci Geo Abstracts 16(1):23–35. https://doi.org/10.1016/0148-9062(79)90772-1

Kranz RL, Scholz CH (1977) Critical dilatant volume of rocks at the onset of Tertiary creep. J Geophys Res 82:4893–4898. https://doi.org/10.1029/JB082i030p04893

Lajtai EZ (1974) Brittle fracture in compression. Int J Fract 10:525–536. https://doi.org/10.1007/BF00155255

Li D, Ma J, Wan Q (2021) Effect of thermal treatment on the fracture toughness and subcritical crack growth of granite in double-torsion test. Eng Fract Mech 253:107903. https://doi.org/10.1016/j.engfracmech.2021.107903

Lisjak A, Grasselli G, Vietor T (2013) Continuum-discontinuum analysis of failure mechanisms around unsupported circular excavations in anisotropic clay shales. Int J Rock Mech Min Sci 65:96–115. https://doi.org/10.1016/j.ijrmms.2013.10.006

Lockner D (1993) Room temperature creep in saturated granite. J Geophys Res 98:475–487. https://doi.org/10.1029/92JB01828
Ma J, Li D, Luo P (2022) Subcritical crack growth and fracture behavior of rocks and long-term strength estimation. Theor Appl Frac Mech 122:103664. https://doi.org/10.1016/j.tafmec.2022.103664
Martin CD, Chandlert NA (1994) The progressive fracture of lac du bonnet granite. Int J Rock Mech Min Geo Abs 31(6):643–659. https://doi.org/10.1016/0148-9062(94)90005-1
Meredith PG, Atkinson BK (1983) Stress corrosion and acoustic emission during tensile crack propagation in Whin Sill dolerite and other basic rocks. Geophys J Roy Astron Soc 75:1–21. https://doi.org/10.1111/j.1365-246X.1983.tb01911.x
Meredith PG, Atkinson BK (1985) Fracture toughness and subcritical crack growth during high-temperature tensile deformation of Westerly granite and Black gabbro. Phys Earth Planet Inter 39(1):33–51. https://doi.org/10.1016/0031-9201(85)90113-X
Modiriasari A, Bobet A, Pyrak-Nolte LJ (2017) Active seismic monitoring of crack initiation, propagation, and coalescence in rock. Rock Mech Rock Eng 50:2311–2325. https://doi.org/10.1007/s00603-017-1235-x
Moradian Z, Einstein HH, Ballivy G (2016) Detection of cracking levels in brittle rocks by parametric analysis of the acoustic emission signals. Rock Mech Rock Eng 49:785–800. https://doi.org/10.1007/s00603-015-0775-1
Musial S, Nowak M, Maj M (2019) Stress field determination based on digital image correlation results. Arch Civil Mech Eng 19:1183–1193. https://doi.org/10.1016/j.acme.2019.06.007
Mutaz E, Serati M, Williams DJ (2024) Crack mode-changing stress level in porous rocks under polyaxial stress conditions. Acta Geotech 19(2):783–803. https://doi.org/10.1007/s10064-021-02187-5
Nara Y, Takada M, Mori D (2010) Subcritical crack growth and long-term strength in rock and cementitious material. Int J Fract 164:57–71. https://doi.org/10.1007/s10704-010-9455-z
Nara Y, Kashiwaya K, Nishida Y, Ii T (2017) Influence of surrounding environment on subcritical crack growth in marble. Tectonophysics 706:116–128. https://doi.org/10.1016/j.tecto.2017.04.008
Nicksiar M, Martin CD (2012) Evaluation of methods for determining crack initiation in compression tests on low-porosity rocks. Rock Mech Rock Eng 45:607–617. https://doi.org/10.1007/s00603-012-0221-6
Paraskevopoulou C, Perras M, Diederichs M (2018) Time-dependent behavior of brittle rocks based on static load laboratory tests. Geotech Geol Eng 36:337–376. https://doi.org/10.1007/s10706-017-0331-8
Park CH, Bobet A (2009) Crack coalescence in specimens with open and closed flaws: a comparison. Int J Rock Mech Min 46:819–829. https://doi.org/10.1016/j.ijrmms.2009.02.006
Ran H, Guo Y, Feng G et al (2021) Creep properties and resistivity-ultrasonic-AE responses of cemented gangue backfill column under high-stress area. Int J Min Sci Technol 31:401–412. https://doi.org/10.1016/J.IJMST.2021.01.008
Renard F, Kandula N, McBeck J, Cordonnier B (2020) Creep burst coincident with faulting in marble observed in 4-D synchrotron X-ray imaging triaxial compression experiments. J Geophys Res Solid Earth 125(9):e2020JB020354. https://doi.org/10.1029/2020JB02035
Scholz CH (1968) Mechanism of creep in brittle rock. J Geophys Res 73:3295–3302. https://doi.org/10.1029/JB073i010p03295
Shabani F, Asadizadeh M, Hedayat A, Tunstall L, Gorman BP, Taboada Neira M, Vega González J A, Verá Alvarado JW (2023) Production of ceramic from sulfidic mine tailings and investigation of fracture toughness under mode I loading. In: ARMA US rock mechanics/geomechanics symposium. ARMA. pp. ARMA-2023
Shen B (1995) The mechanism of fracture coalescence in compression-experimental study and numerical simulation. Eng Fract Mech 51(1):73–85. https://doi.org/10.1016/0013-7944(94)00201-R
Shirole D, Hedayat A, Walton G (2019) Experimental relationship between compressional wave attenuation and surface strains in brittle rock. J Geophys Res Solid Earth 124:5770–5793. https://doi.org/10.1029/2018JB017086
Shirole D, Hedayat A, Walton G (2020) Illumination of damage in intact rocks by ultrasonic transmission-reflection and digital image correlation. J Geophys Res Solid Earth 125(7):e2020JB019526. https://doi.org/10.1029/2020JB019526
Shirole D, Walton G, Hedayat A (2020b) Experimental investigation of multi-scale strain-field heterogeneity in rocks. Int J Rock Mech Min 127:104212. https://doi.org/10.1016/j.ijrmms.2020.104212
Shirole D, Hedayat A, Ghazanfari E, Walton G (2020c) Evaluation of an ultrasonic method for damage characterization of brittle rocks. Rock Mech Rock Eng 53:2077–2094. https://doi.org/10.1007/s00603-020-02045-y
Sinha S, Walton G (2020) A study on bonded block model (BBM) complexity for simulation of laboratory-scale stress-strain behavior in granitic rocks. Comput Geotech 118:103363. https://doi.org/10.1016/j.compgeo.2019.103363
Sone H, Zoback MD (2014) Time-dependent deformation of shale gas reservoir rocks and its long-term effect on the in situ state of stress. Int J Rock Mech Min 69:120–132. https://doi.org/10.1016/j.ijrmms.2014.04.002
Stacey TR (1981) A simple extension strain criterion for fracture of brittle rock. Int J Rock Mech Min Geo Abs 18:469–474. https://doi.org/10.1016/0148-9062(81)90511-8
Sun C, Jin C, Wang L, Cai J, Li J (2023) Creep damage characteristics and slip law of weak-layer mudstone in an open mining slope. Bull Eng Geol Env 82(10):399. https://doi.org/10.1007/s10064-023-03414-x
Sutton MA, Orteu JJ, Schreier H (2009) Image correlation for shape, motion and deformation measurements: basic concepts, theory and applications. Springer Science & Business Media, Cham
Swift GM, Reddish DJ (2005) Underground excavations in rock salt. Geotech Geol Eng 23:17–42. https://doi.org/10.1007/s10706-003-3159-3
Tal Y, Evans B, Mok U (2016) Direct observations of damage during unconfined brittle failure of Carrara marble. J Geophys Res Solid Earth 121:1584–1609. https://doi.org/10.1007/s10706-003-3159-3
Traore S, Naik Parrikar P, Mokhtari M (2023) Full-Field creep mapping in a heterogeneous shale compared to a sandstone. Rock Mech Rock Eng 56:89–108. https://doi.org/10.1007/s00603-022-03073-6
Voigtländer A, Leith K, Krautblatter M (2018) Subcritical crack growth and progressive failure in Carrara Marble under wet and dry conditions. J Geophys Res Solid Earth 123:3780–3798. https://doi.org/10.1029/2017JB014956
Wang Z, Gu L, Zhang Q, Jang BA (2021) Influence of initial stress and deformation states on the shear creep behavior of rock discontinuities with different joint roughness coefficients. Rock Mech Rock Eng 54:5923–5936. https://doi.org/10.1007/s00603-021-02633-6
Wang J, Yang S, Qi Y, Cong Y (2023) Creep characteristics and damage model of coal–rock combinations with different height ratios. Sci Rep 13(1):23072. https://doi.org/10.1038/s41598-023-49841-4
West I, Walton G (2023) Quantitative evaluation of the effects of input parameter heterogeneity on model behavior for bonded block models of laboratory rock specimens. Rock Mech Rock Eng 56(10):7129–7146. https://doi.org/10.1007/s00603-023-03248-9
Wong LNY, Einstein HH (2008) Systematic evaluation of cracking behavior in specimens containing single flaws under uniaxial compression. Int J Rock Mech Min 46(2):239–249. https://doi.org/10.1016/j.ijrmms.2008.03.006

Xue Y, Xu T, Heap MJ (2023) Time-dependent cracking and brittle creep in macrofractured sandstone. Int J Rock Mech Min 162:105305. https://doi.org/10.1016/j.ijrmms.2022.105305

Yao W, Cai Y, Yu J (2019) Experimental and numerical study on mechanical and cracking behaviors of flawed granite under triaxial compression. Measurement 145:573–582. https://doi.org/10.1016/j.measurement.2019.03.035

Zafar S, Hedayat A, Moradian O (2022a) Micromechanics of fracture propagation during multistage stressr and creep in brittle rocks. Rock Mech Rock Eng 55:7611–7627. https://doi.org/10.1007/s00603-022-03045-w

Zafar S, Hedayat A, Moradian O (2022b) Evolution of tensile and shear cracking in crystalline rocks under compression. Theor Appl Fract Mech 118:103254. https://doi.org/10.1016/j.tafmec.2022.103254

Zafar S, Hedayat A, Li BQ, Moradian O (2023) Brittle creep and associated acoustic emissions in granite under unconfined compression. In: 57th US rock mechanics/geomechanics symposium. https://doi.org/10.56952/ARMA-2023-0781

Zhao K, Xiong L, Xu Y et al (2020) Uniaxial compression creep and acoustic emission characteristics of sandstone under loading-unloading paths. Arab J Geosci 13:1243.https://doi.org/10.1007/S12517-020-06240-7

Zheng H, Cao S, Yuan W et al (2022) A time-dependent hydro-mechanical coupling model of reservoir sandstone during CO_2 geological storage. Rock Mech Rock Eng 55:5845–5861. https://doi.org/10.1007/s00603-022-02941-5

Zhou X, Pan X, Berto F (2022) A state-of-the-art review on creep damage mechanics of rocks. Fatigue Fract Eng Mater Struct 45:627–652. https://doi.org/10.1111/ffe.13625